Università` degli Studi di Napoli Federico II

"Microscale investigation of complex liquids in porous media"

Raffaele Graziano

A research project sponsored by

Procter&Gamble

Supervised by:

Prof. Stefano Guido, Prof. Giovanna Tomaiuolo, Valentina Preziosi, Jan Claussen

A thesis presented for the degree of Doctor of Philosophy in Industrial Products and Processes Engineering

March 2021

List of contents

1 Abstract

The interaction of Non-Newtonian fluid and porous media is a topic of great scientific interest and it finds application in a wide number of industrial fields: from the enhanced oil recovery to the drug delivery. In particular, a very interesting category of liquids are the so-called property called “yield stress fluids”. These systems have the ability to behave as solids under this stress threshold and to flow as liquid above it. Numerous studies have been performed in this sense even if the mechanism on a microscale level still have not been completely elucidated.

In this work, we identified some model systems such as polyacrylic acid (Carbopol)-water solutions and by the use of confocal microscopy we looked at the microstructure of the gel to understand the origin of the yield stress and how the confinement and the flow have an impact on this microstructure. It has been observed that the swollen particles of Carbopol build a 3D network whose connectivity causes the yield stress. Furthermore, the system can be described as two phases at equilibrium since the particle concentration does not influence the properties of the solvent phase. Changing the temperature, a phase diagram has been drafted finding analogies with typical polymeric systems, finding a miscibility gap. These learnings helped developing a novel experimental tool,

based on a torsion pendulum equipped with a magnetic dipole and a rotating cylinder immersed in the material, to measure yield stress in gels able to discriminate dynamic and static yield stress.

At the end, an alternative system as detergent foams, has been studied focusing on the process of formation in sponges, in order to understand the effect of surfactant and sponge material on the foamability of the system.

Our experimental data revealed that using a lower confinement in the foam formation allows the production of a drier foams (i.e. with lower liquid fraction, $\varphi L<0.3$), more similar to the ones obtained in dish-washing applications.

Our results are of potential interest for the optimization of foams in complex structures, such as in deformable porous media.

2 Motivation

The aim of the PhD, based on the collaboration with the company Procter and Gamble, was to investigate the world of yield stress fluids and their interaction with porous media. The thesis has been structured in chapters each related to a topic that it has been published or is under the writing phase of the paper. After an introduction on complex liquids and the description of materials and methods used, most of the first section is dedicated to polyacrylic acid solutions since it has been the most studied system all over the duration of the PhD.

Polyacrylic acid, whose trade name is Carbopol, is a polymer extremely interesting for its numerous applications both in industrial and scientific fields since it is a gel with peculiar rheological properties. In this regard, the first results, shown in the 4th chapter, regard the experimental observations on the microstructure of neutralized Carbopol in water using confocal microscopy in static condition. A Carbopol-rich phase made by swollen particles dispersed in a water-rich continuous phase is found, so that the system will be henceforth referred to as a suspension, as long as particles are observed. The swollen particles form dendritic-like aggregates which span the entire solution volume above a critical concentration. In such conditions, a percolated network can be formed, leading to the onset of a yield stress behavior. By separating the dispersed and continuous

phase through centrifugation, we provide evidence of a miscibility gap in the phase behavior of Carbopol in water.

A temperature behavior characterization has been performed in the following chapters to clarify the thermodynamic of the system. A phase diagram has been drafted combining microscopy and rheology, finding a typical UCST trend.

In the 7th chapter microscopy was used to understand the flow properties of these gels. When the Carbopol suspensions flow in a microfluidic capillary, a particle-concentrated plug core can be distinguished from a less concentrated layer corresponding to a steep velocity decrease. Confocal imaging also shows that the apparent slip found in Carbopol suspensions is due to a particle-concentrated near-wall region, where no flow is observed. Such flow-induced microstructure is responsible for the different nature of the yield stress values measured by classical rheometry and by flow velocimetry. While the yield stress measured by the former can be here related to the presence of a percolated network, the yield stress obtained from the velocity profile is due to the heterogeneous particle distribution along the capillary radius. These results provide a novel insight on the mechanisms governing yield stress in complex fluids.

Thanks to the collaboration with the Department of Physics of the Federico II University the investigation in the Carbopol world has also been carried out using

a novel instrument to evaluate yield stress. It is based on a torsion pendulum equipped with a magnetic dipole and a rotating cylinder immersed in the material to be investigated. The pendulum equilibrium state depends on the mechanical torque applied due to an external magnetic induction field, elastic reaction of the suspension wire and shear yield stress. Experimental results reported show that the behavior of the pendulum rotation angle, in different equilibrium conditions, provides evidence of the yield stress presence and enables its evaluation by equilibrium equations. The validity of the proposed technique and related experimental apparatus were tested in aqueous Carbopol solutions, with different weight percentages.

In the last chapter, a work where the foam formation in kitchen sponges is studied using microscopy is presented. Foams, at certain volume fraction, can been described as yield stress systems, that are formed in very complicated porous media, where in fact the deformability cannot be neglected. The investigation about foam formation in deformable porous media was carried out by using sponges as a model system, with a special emphasis on the effect of confinement on foam bubble size distribution. Foam was formed by wetting the sponge with an aqueous surfactant solution and then squeezing the sponge either between two glass coverslides or between a plastic net and a coverslide. Our experimental data

reveal that the latter system allowed the formation of drier foams (i.e. higher volume fraction) more similar to the ones obtained in dish-washing applications. Moreover, the effect of sponge type, in terms of material and microstructure, on final foam is presented. Therefore, our results are of potential interest for the optimization of foams in complex structures, such as in deformable porous media.

3 State of the Art

Soft matter refers to a vast family of systems which are ubiquitous in our everyday life, such as polymers, colloids, emulsions, foams, gels, and biological fluids [1]. The common feature of such materials is the physical response to applied stresses, that is neither typical of a Newtonian liquid nor of an elastic solid. Soft matter, also known as complex fluids, can exhibit non-Newtonian properties like shear thinning/thickening (i.e. viscosity is a decreasing/increasing function of shear rate), stringiness (i.e. high extensional viscosity) and yield stress, a threshold value of stress below which the material behaves as an elastic solid and above which flows as a viscous fluid [2, 3]. This latter property makes yield stress fluids suitable for a wide range of uses, from daily products, such as food (i.e. mayonnaise, ketchup, dairy), cosmetics (i.e. toothpaste, body lotions) and pharmaceutics (cough syrup,

analgesic cream) to industrial applications, such as concrete, 3D printing, oil recovery and transport [4]. Given the widespread applications, a number of reviews [1, 5-7] and original papers focusing on yielding behavior can be found in the literature, concerning rheological characterization [8-10] or aimed at the interpretation of the physical processes occurring at the micro-scale [11, 12]. Before going into the detail of the present work it is necessary to stress out the concept of complex liquids.

3.1 Non-Newtonian fluids

A non-Newtonian (or complex) fluid is characterized by shear stress (τ_{yx}) – shear rate ($\dot{\gamma}_{yx}$) functionality which does not obey the Newton – Stokes linear relation (1). Deviations can be represented by the absence of linearity or by a stress – rate plot (the so-called *flow curve*) that doesn't intercept the origin.[13]

The Newton – Stokes relation is the following:

$$\tau_{yx} = \eta\, \dot{\gamma}_{yx} \qquad \textbf{(1)}$$

where the subscripts indicate respectively the direction normal to that of shearing surface and the one of both the applied force and the flow, whereas the constant

of proportionality is the so called “Newtonian viscosity” (η) and is, by definition, only dependent on material’s nature, temperature and pressure. For non-Newtonian fluids, the ratio between shear stress and shear rate is termed “apparent viscosity” and can be both a function of time and rates. It is clear that these materials can exhibit a very wide array of behaviours.

During the past five decades, there has been a growing recognition of the fact that many substances of industrial significance, especially of multi-phase nature (for example foams, emulsions, dispersions, suspensions or slurries) and polymeric melts and solutions conform to the definition of non-Newtonian fluid [14], even though the interest in such substances had birth in the early 1900’s, when many scientists, among them Bingham, found that many colloidal suspensions and polymer solutions give a viscosity that decreases with increasing shear rates [15]. Table 1 shows a list of substances exhibiting non-Newtonian fluid behaviour.

■ Adhesives (wall paper paste, carpet adhesive, for instance) ■ Ales (beer, liqueurs, etc.) ■ Animal waste slurries from cattle farms ■ Biological fluids (blood, synovial fluid, saliva, etc.) ■ Bitumen ■ Cement paste and slurries ■ Chalk slurries ■ Chocolates ■ Coal slurries ■ Cosmetics and personal care products (nail polish, lotions and creams, lipsticks, shampoos, shaving foams and creams, toothpaste, etc.) ■ Dairy products and dairy waste streams (cheese, butter, yogurts, fresh cream, whey, for instance) ■ Drilling muds ■ Fire fighting foams	■ Foodstuffs (fruit/vegetable purees and concentrates, sauces, salad dressings, mayonnaise, jams and marmalades, ice-cream, soups, cake mixes and cake toppings, egg white, bread mixes, snacks) ■ Greases and lubricating oils ■ Mine tailings and mineral suspensions ■ Molten lava and magmas ■ Paints, polishes and varnishes ■ Paper pulp suspensions ■ Peat and lignite slurries ■ Polymer melts and solutions, reinforced plastics, rubber ■ Printing colours and inks ■ Pharmaceutical products (creams, foams, suspensions, for instance) ■ Sewage sludge ■ Wet beach sand ■ Waxy crude oils

Table 1: Non-Newtonian fluid behaviour substances [13]

Chhabra and Richardson have proposed a helpful categorization for complex fluids features, grouping them in three general classes [16]:

1. *Generalized Newtonian fluids (GNF)*: materials for which the shear stress is point-by-point dependent only on the shear rate. These fluids are also known as *time-independent*, *purely viscous* or *inelastic*;

2. *Time-dependent fluids*: here the relation between stress and shear rate depends also on the duration of shearing and the kinematic history of the material;

3. *Viscoelastic fluids*: the properties of these substances lie in the middle between elastic solids and viscous liquids, showing partial elastic recovery after deformation.

The presented categories are not meant to be independent one to another: indeed, most real fluids belong to two or even all the three classes proposed.

Based on this classification, we will present the most relevant non-Newtonian behaviours for our research, correlated with the mathematical models of interest.

3.2 Time-independent fluid behaviour

In these class of fluids, the value of the stress is determined only by the punctual value of the shear rate. According to the functional form of $\tau_{yx} = f(\dot{\gamma}_{yx})$, there exist three subgroups. From now on we will simplify the notation by removing subscripts *yx* for both stress and shear rate.

- Shear-thickening or dilatant fluids

These fluids are characterized by an increasing apparent viscosity with the increase of the shear rate and are not very common in chemical and processing industries.

- Shear-thinning or pseudoplastic fluids

Shear-thinning (or pseudoplastic) behaviour is typical of complex fluids whose apparent viscosity decreases with shear rate. Many ordinary substances belong to this time-independent subgroup, such as glues, polymer solutions and melts or shampoos. Even though it is possible to refer to such fluids with both the terms "shear-thinning" and "pseudoplastic", in agreement with Bingham and Ostwald [17, 18], the former is way more common and must not be confused with time-dependent viscosity diminution at constant shear rate, termed "thixotropy".

On a wide shear rate range, shear-thinning fluids usually present two Newtonian regions, respectively at very low and very high $\dot{\gamma}$ values. The apparent viscosity – shear rate plot (viscosity curve) in *log-log* scale will therefore be characterized by three zones as in *Figure 1*:

1. The first Newtonian plateau, where $\eta_0 = \lim_{\dot{\gamma}\to 0} \eta(\dot{\gamma})$ is the *zero-shear* viscosity;
2. The shear-thinning range, where the apparent viscosity is a decreasing function of the shear rate;
3. The second Newtonian plateau, where $\eta_\infty = \lim_{\dot{\gamma}\to \infty} \eta(\dot{\gamma})$ is the *infinite-shear* viscosity.

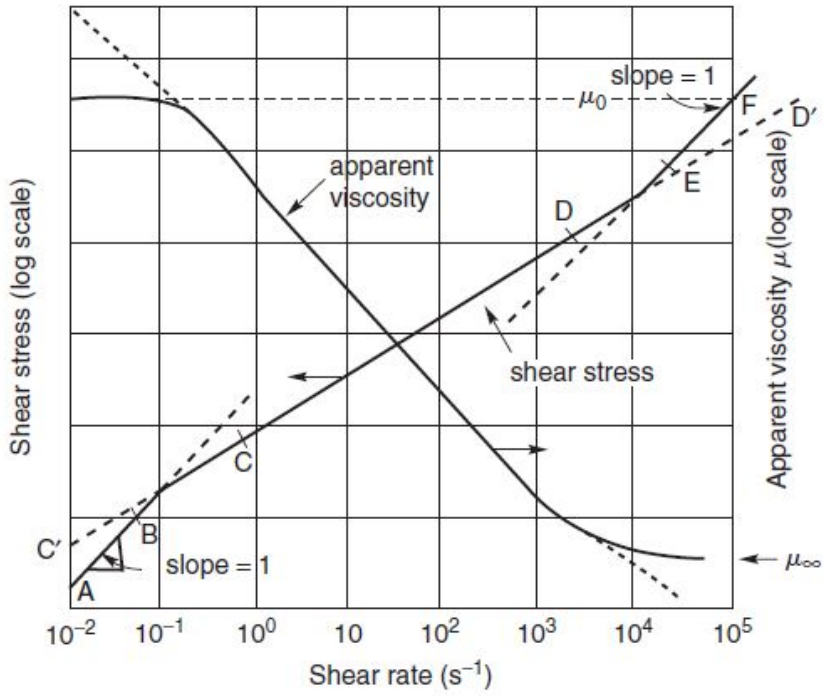

Figure 1: Schematic representation of shear-thinning behaviour [16]

For polymer solutions, the zero-shear Newtonian plateau can be obtained only if the polymer concentration is high enough to allow the formation of entanglements [19].

The definition of the "overlap concentration" (c^*), let us distinguish between the cases of dilute and concentrated polymer solutions. Such concentration indicates the critical one where the effective volumes occupied by the component polymer coils, related to the radii of gyration (R_g), begin to touch [20]. Below c^* the solution is dilute and polymer coils do not touch each other; in these range,

polymers behave as hard spheres of radius R_g because of the high energy required for overlapping [21]. Low concentrated solutions with absence of effective entanglements between molecule chains display ideally viscous flow behaviour, where the viscosity value is directly proportional to the concentration [19]. Above c^*, coils start interpenetrating and sharing volumes with neighbouring polymer chains. Here, with increasing concentration, there is a stronger increase of the zero-shear viscosity, as one can see from the higher slope of $\eta_0(c)$ in this concentration range (Figure 2). The different regimes are illustrated too: (a) dilute regime at $c < c^*$, (b) critical case at $c = c^*$, (c) concentrated regime at $c > c^*$.

Zero-shear viscosity depends also on the average molar mass (*M*), which, as like as concentration in polymer solutions, influences the formation of effective entanglements between the macromolecules [22].

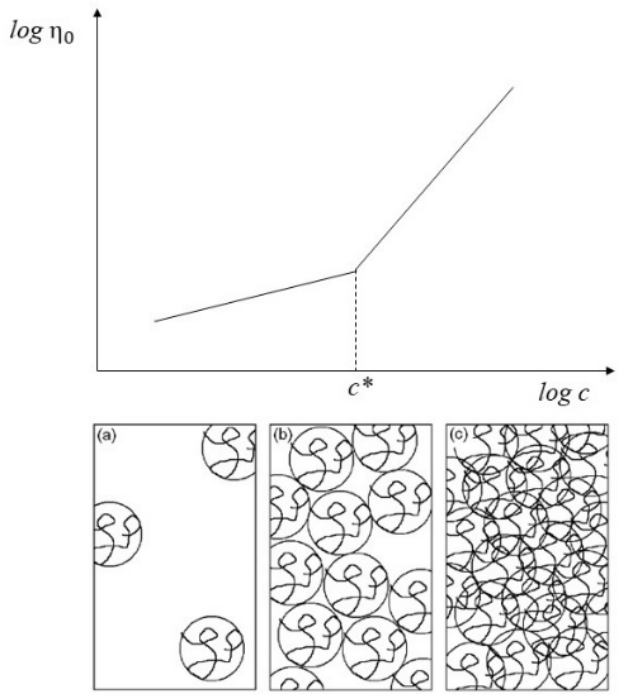

Figure 2: Dependence of low shear viscosity on the polymer concentration and illustration of concentration regimes

In the shear-thinning range, the more the shear rate increases, the more the number of disentanglements exceeds the number of re-entanglements, resulting in a reduction of viscosity. The complete orientation and disentanglement of all polymer coils explains the high-shear Newtonian plateau, where the flow resistance is reduced its minimum.

Let us now examine two widespread mathematical relations proposed in the literature to model shear-thinning fluid behaviour.

The first one is the *power-law* or *Oswald de Waele* model [23]. This relation well describes the shear-thinning region, that on a double logarithmic scale flow curve (or viscosity curve) corresponds to a straight line. For this part the following expressions for stress and apparent viscosity are applicable:

$$\tau = k \cdot \dot{\gamma}^n \qquad \textbf{(2)}$$

$$\eta = k \cdot \dot{\gamma}^{n-1} \qquad \textbf{(3)}$$

k and *n* are two empirical parameters respectively known as "fluid consistency coefficient" and "flow behaviour index". The latter allows to discriminate whether the fluid is Newtonian ($n = 0$), shear-thinning ($n < 1$) or shear-thickening ($n > 1$). The main drawback of the power-law model is its limitation to a very limited range of shear rates, affecting the parameters' estimation quality. Moreover, it doesn't predict the low and high shear rate Newtonian plateau, therefore it is useless when dealing with the above-mentioned polymer solutions.

To overcome these problems, one could use the *Carreau viscosity equation*. This model is based on Carreau's molecular network considerations [24] and incorporates both η_0 and η_∞:

$$\frac{\eta-\eta_\infty}{\eta_0-\eta_\infty} = [1 + (a \cdot \dot{\gamma})^2]^{(n-1)/2} \qquad \textbf{(4)}$$

Where $n < 1$ and a are two curve-fitting parameters. The presence of four parameters is helpful in fitting curves over a wide range of shear rate; it is, however, important to use it prudently, assuring that each parameter has physical meaning.

A separate section will be dedicated to the third time-independent fluid behaviour subgroup, *visco-plastic fluids*.

3.3 Viscoelastic behaviour

According to Macosko, *viscoelasticity* is a time-dependent response typical of materials such as gum rubber, pitch and polymeric materials, which under a shear (or extensional) loading present an instantaneous deformation followed by a continuous one called “creep” [15]. In order to better understand what these substances are, it could be helpful to briefly analyse the response of an ideal solid and a Newtonian fluid to a stress.

A perfect solid, subject to a load, reacts deforming instantly and then regaining its original form upon the removal of the stress. This is true if the applied force lays under a yield value so that the Hooke’s linear relation between stress and deformation is still valid; in this case the deformation is called “elastic”. On the

other side, an ideally viscous fluid would show a continuous deformation with no reformation after the load's removal, since it is not able to store any deformation energy during the load phase. The resulting deformation of a viscoelastic material under a constant stress consists of two portions in succession. The former occurs immediately and consists in a rising deformation; the latter is a delayed reformation that takes place as the load is removed and its extent depends on the elastic portion of the material: a viscoelastic solid completely recovers its shape after an adequate testing time, a viscoelastic liquid, instead, remains partially deformed. However, the response of such materials, depends not only on their structure but also on the kinematic conditions they have been subject to. Viscoelastic materials lie, therefore, in between elastic solids and viscous liquids, which are in practical terms limiting cases of viscoelastic behaviour. They are characterized by an elastic and a viscous portion that in turn prevail and define if the behaviour is *liquid like* or *solid like*.

3.4 Yield stress fluids: visco-plastic behavior

These unique class of materials is characterized by the presence of a stress threshold (τ_y) under which the material deforms like an elastic solid. On the other side, at values above τ_y the fluid will flow and behave either like a Newtonian fluid or a complex one; in both cases the flow curve will not pass through the

origin. Consequently, if surface tension effects are not relevant, such materials will not form a flat surface when levelling under the action of gravity, nor a drop on a tilted surface will flow down.

This property makes these fluids extremely suitable for a wide range of applications: thanks to the yield stress it is possible to decorate cakes with whipped cream, contain the leakages of coatings and glues during their application or keeping particles and droplets suspended [25].

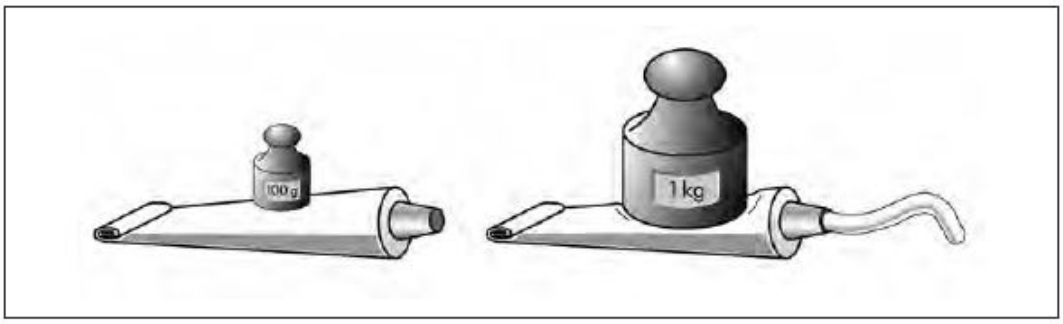

Figure 3: Toothpaste - our daily struggle with the yield stress [19]

The yield stress is originated by the existence of a rigid microstructure which resists to any external stress lower than the yield one. Above this point the fluid is submitted to flow, and a partial destruction of the inner structure occurs causing a drop in the viscosity, as observed in rheological tests that evidence a thixotropic behaviour. Moreover, many yield stress systems at rest show a spontaneous

reformation or evolution of the microstructure, a process called “aging”; this leads to a possible increase of an apparent yield stress with time [26].

This mechanical response has been associated with a bifurcation in the rheological behaviour: for small stresses, there is a viscosity increase over time and the material stops flowing eventually. For moderately larger stresses, viscosity starts decreasing in time and the flow accelerates. There is, therefore, a discontinuity as the viscosity tends to infinity approaching the critical stress [27] (*Figure 4*).

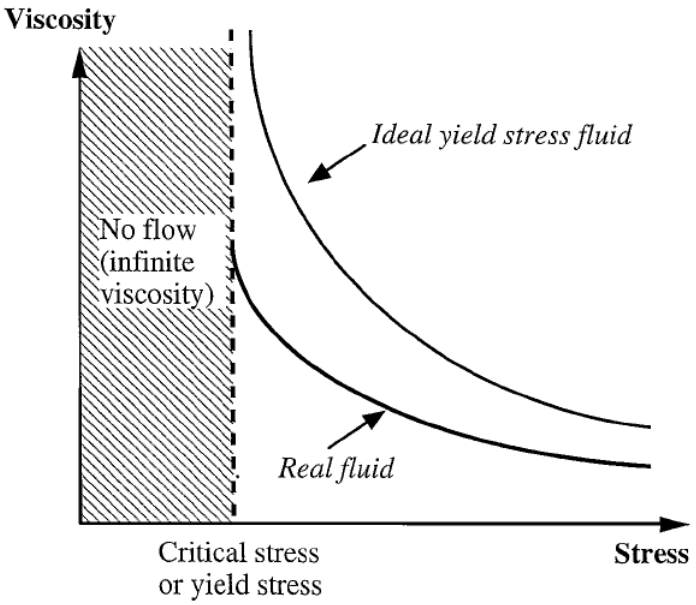

Figure 4: Schematic representation of the viscosity-stress curve for an ideal yield stress fluid and a real fluid

Nonetheless, there has been a controversy about whether the yield stress marks a transition between a solid and a fluid state, or between two fluid states with

considerably different viscosities and several experimental studies testify that yield stress materials actually behave like Newtonian liquids at low stresses [1]. H. A. Barnes and Walters presented data on Carbopol microgels to demonstrate the existence of a finite viscosity at very low shear stresses, therefore demonstrating the absence of any discontinuity nearby the critical stress value [28].

Let us now examine the two possible cases of visco-plastic materials: *Bingham plastic* and *yield-pseudoplastic* fluids.

3.5 Bingham plastic fluids

These fluids are characterized by a constant plastic viscosity, therefore a linear flow curve (Newtonian behaviour) for $\tau > \tau_y$. The simplest mathematical model describing the flow behaviour of such substances in steady one-dimensional shear, is the *Bingham plastic model*:

$$\begin{aligned} \tau &= \tau_y + \mu_B(\dot{\gamma}) \quad for \quad \tau \geq \tau_y \\ \dot{\gamma} &= 0 \qquad\quad for \quad \tau < \tau_y \end{aligned} \tag{8}$$

As written by Bingham in his original paper, allowing no motion below the yield stress [17].

3.6 Yield-pseudoplastic fluids

Upon the critical stress value, these fluids show a non-linear flow curve, thus a shear-thinning behaviour. A generalization of the Bingham plastic model has been proposed by Herschel and Bulkley [29]:

$$\begin{aligned} \tau &= \tau_y + m(\dot{\gamma})^n \quad for \quad \tau \geq \tau_y \\ \dot{\gamma} &= 0 \qquad\quad for \quad \tau < \tau_y \end{aligned} \tag{9}$$

With the m and n (< 1) parameters of similar meaning to those in the power-law model (2).

Despite many efforts have been devoted to the understanding of the yield stress phenomenon, the concept and the existence itself of yield stress has been debated for a long time [9, 28], mostly due to the scarcity of reliable and reproducible measurement methods [30]. Beyond technical issues, the main problem lies in the physical-chemical origin of the solid-liquid transition underlying yield stress, that is yet to be fully elucidated.

3.7 Rheology and Yield stress measurement

Generally, the test used to present the differences between viscoelastic materials and ideal solids and liquids is called “creep test”. This is performed by applying two shear stress steps and measuring the strain as a function of the time (t); from

t_0 to t_2 the stress value is equal to τ_0, while from t_2 to t_4 it constantly zero, as in *Figure 5*.

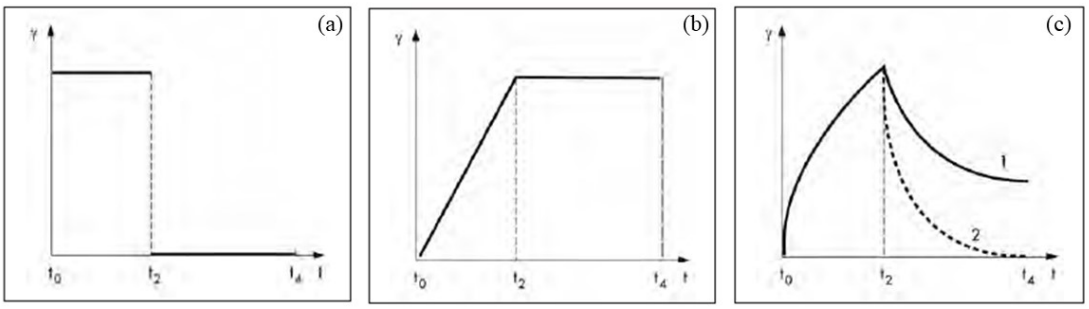

Figure 5: Creep and creep recovery of (a) an ideally elastic solid, (b) an ideally viscous liquid, (c)-1 a viscoelastic liquid and (c)-2 a viscoelastic solid

Creep data are usually expressed in terms of compliance $J(t)$:

$$J(t) = \frac{\gamma(t)}{\tau_0} \qquad \textbf{(5)}$$

There exist other two techniques one could be performed to analyse the viscoelastic behaviour: *stress relaxation* and *sinusoidal oscillations*. Before proceeding with their description, it is important to point out that all these tests are performed in the *linear viscoelastic region*. Here, the experiments are performed in a range of small strains so that no irreversible modification affects the material's structure. In this region all the tests must be related to one another through the

relaxation modulus, defined in (6), which is independent of strain. However, transforming results from on experiment type to another is often not easy [15].

$$G(t) = \frac{\tau(t)}{\gamma} \qquad \textbf{(6)}$$

Stress relaxation is the easiest method to determine $G(t)$. It is performed applying a strain step on the material and observing the stress response over time.

In the *sinusoidal oscillations* method, the sample is deformed sinusoidally, resulting in a likewise oscillating stress response that will be shifted of a phase angle δ. The decomposition of the stress response in its two components, respectively in phase and 90° out of phase, leads to the definition of the dynamic moduli, which are essential in the characterization of the material as we will see in the results section. The in-phase component is related to the *elastic modulus* G' and expresses the elastic portion of viscoelastic behaviour; the *viscous modulus* G'', instead, corresponds to the out-of-phase component, linked to the viscoelastic behaviour's viscous portion. The two moduli are also termed "storage" and "loss", making clearer their relation to the potentiality of the material to elastically store or viscous dissipate the deformation energy provided by the strain. Another useful parameter is the ration between G'' and G', known as "damping factor":

$$\tan\delta = {}^{G''}/_{G'} \qquad \textbf{(7)}$$

The damping factor allows us to discriminate whether the material is solid like ($\tan\delta < 1$ and $G' > G''$), liquid like ($\tan\delta > 1$ and $G' < G''$), or at the sol-gel transition point ($\tan\delta = 1$ and $G' = G''$). The ideal solid and liquid behaviours correspond to $\tan\delta \to 0$ and $\tan\delta \to \infty$, respectively.

This mode of testing is also referred to as dynamic mechanical analysis (DMA) and is used to examine all kinds of viscoelastic materials [19].

3.8 Yield stress determination

Knowing the value of the yield stress is crucial in industrial applications; it is indeed related to the minimum pressure needed to start the flow of a slurry in a pipeline, but also to assess the sensory properties (e.g. consumer tactical perception) of foods or cosmetics [31, 32]. Many methods have been proposed for the determination of the yield stress, even though it has been demonstrated that variation of different order of magnitude can occur depending on the chosen method and the handling of the sample [33]. These discrepancies have conducted to the distinction of two types of critical stress. The former is the *static yield stress*,

defined as the minimum stress the material needs to start flowing; the latter is the *dynamic yield stress*. It is the minimum stress required for maintaining flow and usually has a smaller value [34].

Another classification can be made between *simple* and *thixotropic* yields stress materials. The first category comprehends fluids whose yield stress is well defined and considered a material's property; moreover, their viscosity is a shear rate function only (the aforementioned *time-independent fluid behaviour*). In thixotropic yield stress materials, viscosity is a function of the material's deformation history too. In this case the viscoplastic behaviour is due to the competition between the build-up of a microstructure and the shear breakdown of triggered by the flow [1]. The works of Balmforth and Coussot show that while or simple yield stress materials both static and dynamic critical stress coincide, for the thixotropic ones the two values are non-identical [5, 35].

A first way of determining the yield stress is by using the flow curve diagram, thus performing shear rate or shear stress sweeps. The most classical method is probably the one where shear stress is imposed and increased in to form of steps or as a ramp; here the τ_y value corresponds to the last point at which the measuring device is still detecting no sign of motion and $\dot{\gamma} = 0\ \frac{1}{s}$. Imposing a shear rate, in

lieu of a stress, doesn't lead to a direct determination of the yield stress, which must be inferred using a mathematical model, such as the Herschel-Bulkley model. Anyway, these methods have a drawback: the calculated yield stress depends on the speed resolution of the rheometer [19, 36].

By imposing a shear stress, it is also possible to evaluate the yield stress by the stress-deformation diagram. Here the yield point is the stress value at which the linear-elastic deformation range is exceeded, hence on a double logarithmic plot the slope of $\tau(\gamma)$ doesn't equal to one anymore. τ_y can also be calculated by the interception of a unitary slope line at low strains with a power-law equation at high strains.

Oscillatory techniques are widespread used to measure the yield stress. Performing an *amplitude sweep* (a strain sweep at a fixed oscillation frequency) it is possible to evaluate the dynamic moduli (G' and G'') as a function of the shear stress. Here, the yield stress equals to the limit of the linear viscoelastic range, where the material is showing reversible viscoelastic behaviour and thus the moduli are not dependent on the shear stress. Typically, τ_y is calculated using only the storage modulus curve; the critical value can be obtained observing the deviation of G' from the plateau and selecting an arbitrary range of tolerance (i.e. 5%) [19].

However, as pointed out by Rouyer, a unique criterion to determine the yield stress from oscillatory data does not exist. Indeed he calculates it from the interception between an horizontal line -representing G' above the yielding point- and a power-law equation describing the behaviour of G' above it [37]. Other authors, instead, define the yield stress as the value for which $G' = G''$ [36].

Lastly, the yield stress can be measured by the creep compliance. Here the strain should approach a constant value for imposed stresses below the yield value, while the compliance should start increasing as a function of time for higher stresses. A disadvantage of this technique lays in the fact that one must know in advance the stress range where τ_y is expected.

In our experimental procedure, oscillatory rheology has been used to measure yield stress for Carbopol samples.

3.9 Carbomers as a polyelectrolyte gel

The most widely used fluids for the investigation of yield stress belong to the Carbopol family, that comprises various forms of commercial synthetic thickeners. In the last 50 years, Carbopol-based systems have raised increasing interest in fundamental scientific understanding [30, 38] as well as in industrial applications,

from the study of tectonic faulting [39-41] to personal care [42] and pharmaceutical products [43, 44]. As an example, Carbopol forms biocompatible and FDA approved gels that are widely used in the formulation of drug delivery systems [45-48]. Carbopol polymers (also known as carbomer resins) are high-molecular weight homo-polymers of acrylic acid intramolecularly cross-linked by polyethers [39, 49]. In the dry state, they appear as white powder made by micron-sized particles, but once they are dispersed in water, a slight uncoiling of the molecules occurs. The neutralization with a suitable base lead to a further, stronger uncoiling due to the electrostatic repulsion among the negatively charged pendant carboxylic acid groups which, in turn, results in a dramatic expansion of polymer chains. Indeed, after neutralization, Carbopol particles undergo remarkable particle swelling, even more than 10 times of their initial diameter [30, 39]. In this scenario, Carbopol can be considered as a polyelectrolyte microgel, being made by cross-linked gelled polymer particles interacting among each other by means of the dangling free ends. The resulting physical behavior lies between that of entangled linear polymers and the one of non-interacting hard spheres [50]. This picture is in agreement with recent studies, including micro-rheology measurements, which propose a concentration-dependent rheological response and suggest that a Carbopol aqueous system acts as a suspension at low concentration, as a fluid with a percolated

microstructure at intermediate concentration and as gel made by compressed space-filling microparticles at high concentration [30, 51, 52]. Furthermore, Carbopol-based systems show a viscoelastic behavior both in steady-state (i.e. shear thinning) and oscillatory tests, with the elastic modulus higher than the viscous one for a wide range of frequencies [2, 53]. Carbopol rheological behavior is also strongly sensitive to pH; in particular, neutral pH is associated with the highest yield stress and elasticity, where the system reaches the maximum particle swelling (due to an osmotic flow of the water phase). In this condition, small variation of pH does not affect the rheological response of the sample [11, 54].

One of the most peculiar properties of a Carbopol-based fluid is that it appears as transparent and homogeneous, whereas high yield stress fluids are often rather turbid mostly due to multiple light scattering from their multiphase microstructure (typical examples are ketchup, foams, and toothpaste). The optical transparency of Carbopol can be ascribed to the already mentioned swelling of the particles whose cross-linking is considered at the root of the yielding behavior. As reported in several works [55, 56], whereby different techniques, such as microscopy [12, 54, 56, 57] and light scattering [11, 52] have been exploited, at low polymer concentration the absence of yield stress corresponds to irregular network structures made by diluted swollen micro-gel particles barely interacting with each

other. On the other hand, the presence of yield stress at increasing concentrations has been related to the increase of cross-linking density that leads to percolated space-filling micro-gel structures [30, 54, 56]. However, yield stress can be also related to jamming of high-volume fraction particulate systems, such as emulsions, foams and suspensions [58-60]. It is worthwhile to mention that such studies have correlated images of Carbopol suspensions at different concentrations under *static* conditions with classical bulk rheology yield stress measurements. Recently, microfluidic experiments have been used for the investigation of the effect of confinement on Carbopol microstructure via indirect methods such as flow velocimetry, in order to improve the understanding of the relationship between confined flow and bulk rheology response [57]. In fact, when a complex fluid flows in a device with dimensions comparable to its particles size, the combined effect of shear rate and confined conditions can heavily affect microstructure, in terms of both particle size and polydispersity. The effect can lead to the disruption of the micro-gel structure [57], and is likely responsible of the discrepancy between microfluidic results and bulk rheology [1].

Here, we describe how the microstructure of Carbopol aqueous suspensions can be visualized with unprecedented resolution by confocal microscopy and labeling the water phase with a fluorescent dye. This technique allows one to measure the

particle swelling ratio as well. By coupling confocal microscopy with microfluidics, we show for the first time the effect of confined capillary flow on Carbopol microstructure *in situ*, providing a correlation between particle distribution along capillary radius under flow and yield stress.

4 Material and Methods

Over the lifetime of the PhD the following materials and techniques have been mastered
and used.

4.1 Materials

Polyacrylic acid (Carbopol® 980 NF Polymer) produced by Lubrizol was used to prepare aqueous systems. Firstly, the polymer powder was dissolved in deionized water (Millipore) by mixing with a propeller (Heidolph RZR 2102 Control) for about 15 min at 700 rpm. Secondly, Carbopol was neutralized with sodium hydroxide (supplied by Sigma Aldrich) in water at 1 M concentration while

stirring for about 1 h, until pH 7 was reached. Polyacrylic acid in water was prepared at different concentrations between 0.01% wt and 0.1%wt.

4.2 Confocal Laser Scanning Microscopy

The experiments were carried out by using a confocal laser scanning microscope (LSM 5 Pascal, Zeiss) equipped with a helium/neon laser (LASOS Lasertechnik GmbH, LGK SAN7460A). Experimental observations were performed with a 100x immersion oil objective (Achroplan, Zeiss) with a numerical aperture of 1.25. Fluorescein Isothiocyanate (FITC, Sigma Aldrich) was used as a fluorescent dye and dissolved in water in a 500 μM concentration, and a 488 nm laser was used for excitation. FITC fluorescent signals were detected in the green channel with an optical setup including a LP560 filter and NT80/20 and NFT545 beam splitters. Once the sample with dye was prepared, it was wrapped with aluminum foil and stored into the fridge. In addition, the field of view was changed from time to time to avoid over-exposing the sample to the exciting beam and image fluorescence was measured after each acquisition by using Image-pro-plus software. A high-speed video camera (Phantom 4.3), combined with an optical microscope (Axiovert 100, Zeiss) and a 40x/oil objective (Zeiss), was used to

investigate the behaviour of the Carbopol suspensions under flow. To investigate the fluid velocity profiles, 4 μm diameter polystyrene beads (Sigma Aldrich) were added to Carbopol suspensions as tracers at low concentration, so as not to alter the rheology of the system (0.05 ml of 2.5% (w/v) aqueous dispersion of beads in 50 ml of Carbopol suspension). The Carbopol suspensions were injected into a 320 μm (inner diameter) silica microcapillary (Polymicro Technologies), placed on the stage of the microscope, by a micro-pumping system (Fluigent) allowing one to impose pressure drops ranging from 0.2 to 1 bar.

Confocal microscopy was also used to investigate the flow-induced microstructure of the Carbopol suspensions. To this purpose, imaging was performed after stopping the flow once steady state conditions had been reached. The flow has been interrupted instantaneously using a clap on the connecting tubing, thus "freezing" the microstructure. Image recording have been made in the first few seconds after the stop. The observed morphology was stable and not change was observed throughout the image acquisition time, thus ensuring that stopping the flow did not alter the microstructure.

All the experiments were performed at room temperature. No relevant dependence of rheological behaviour on temperature in the range 20°C - 37°C was found.

In order to evaluate the effect of Carbopol particles on yield stress, fluids were centrifuged (Thermo Scientific MicroCL 17R) several times at 13000 rpm for 40 min to obtain two separated phases: a particle-rich lower phase, and a particle-poor upper phase.

An image processing software (Image Pro Plus 6.0) was used offline for quantitative analysis of the images from the experiments. The volume fraction of the Carbopol rich-phase, both in static conditions and under flow, was taken as equal to the area fraction of the same phase [61]. The software was also used to obtain a composite image by combining all the images in a video sequence from the experiment. The grey level of each pixel in the composite image was taken as the grey level of the image with the minimum local contrast at the pixel in the sequence.

4.3 Rheological measurements

Steady shear measurements were performed by using a stress-controlled Physica rheometer MCR 301 (Anton-Paar, Graz, Austria) with a double-gap configuration (DG 26.7, inner cup diameter 24.267 mm, inner bob diameter 24.666 mm, outer bob diameter 26.663 mm, outer cup diameter 27.053 mm, and bob height: 40.000 mm) for low concentration suspensions (i.e., 0.01 and 0.07 % wt), while a cone-

plate configuration (CP 75 mm, 1°) was used for higher concentrations (i.e. 0.1 % wt). Viscosity tests were carried out in a range of shear rate between 1 and 1000 s^{-1} and at room temperature. Yield stress measurements were performed by oscillatory tests, one of the most used ways for the determination of yield stress [19, 36, 62]. In particular, the yield point has been estimated by taking the 5% deviation from the linear viscoelastic region, corresponding to the initial drop of G′, plotted as a function of shear stress at the frequency of 1 Hz. All the measurements were repeated twice for reproducibility.

4.4 Particle tracking analysis

Particle tracking analysis was carried out by measuring the position of the 4 μm polystyrene beads as a function of time through the Image Pro-plus software. Particles displacement was linear with time and the slope was used to determine the velocity profiles inside the capillary [63]. The image analysis procedure has been described in detail elsewhere [64].

4.5 NMR MOUSE

The device that has been used for the measurements was a PM-25 NMRMOUSE from Magritek (Aachen, Germany) which belongs to the Procter and Gamble Technical Center of Schwalbach am Taunus. It has a depth range varying from 5 to 25 mm, sufficiently large to cover the thickness of different porous materials in this specific case multiple layers of filter paper. The sensitive slice above the surface of the sensor is 4Å~4cm2, and 1D profiles can be acquired across different depth ranges with the help of a high-precision lift. This device generates a static gradient of 8 T/m in the direction perpendicular to the sensor surface, and the protons in the sensitive slice are in resonance at a frequency of 13.5 MHz. The field of view in the z direction was chosen of 50 μm, due to catch possible accumulation of liquid in media interfaces. [65]

Two different pulse sequences were used, a CPMG sequence for T2 relaxation measurements (echo time 150 μs, number of echoes 4096, repetition time 6000 ms, number of scans 8), and a saturation-recovery sequence to measure T1 relaxation (echo time 63.5 μs, number of echoes 256, repetition time 100 ms, number of scans 8, recovery time 9000 ms).

5 The microstructure of Carbopol in water under static conditions

5.1 Microscale investigation using LSM

Carbopol in water appears as a highly transparent material both at the naked eye and in bright field microscopy, a feature which makes imaging of microstructure a non-trivial task. The lack of optical contrast between Carbopol particles and background provides evidence that the former have a refractive index quite close to that of the continuous aqueous phase. Since Carbopol and water have quite different refractive indices, the lack of contrast suggests that Carbopol particles are highly swollen (i.e., full of the aqueous phase). As a consequence, bright field optical imaging is not able to visualize the particles in the suspension even by using high magnification objectives. In previous works, imaging of Carbopol microstructure was achieved by adding positively charged Rhodamine [2, 66] and Acridine Orange [54] dyes, which get rapidly absorbed by the negatively charged Carbopol particles. However, the neutralization step with NaOH leads to leaching out of the dyes, as reported for Acridine Orange [54], and result in a rapid decrease of image contrast. Static visualization of Carbopol suspensions have been also obtained by using Alexa Fluor 488 as a fluorescent day [67]. In any event, the analysis of the structure of neutralized Carbopol suspensions is of great

importance for many applications (i.e. pharmaceuticals) in which viscoelastic and yielding properties, ensured by pH 7, are key factors for specific material features. In our particular case, the problem of having confocal images with enough signal was addressed by labeling the water phase with a neutral fluorescent dye (FITC)[68], which is stable in the neutralized suspension (instead of the direct labeling of Carbopol with cationic dyes, that leads to a rapid decline of image contrast). In Figure 6, confocal images of Carbopol suspensions at four different concentrations (0.01, 0.05, 0.07 and 0.1% wt) are presented, showing well defined black spots of about 3-4 μm against a bright background starting from the 0.05% concentration (the sample is indeed featureless at lower concentrations, such as 0.01%).

As the Carbopol concentration increases, the black spots tend to form aggregates (with size around 10 μm) and develop an extended dendritic-like structure (highlighted by the circle of Figure 6c), which can be expected to have a strong effect on the physical properties of the fluid, including the static yield stress, whose values are also presented in Figure 6, which is caused by the 3D structuration of the Carbopol gel network.

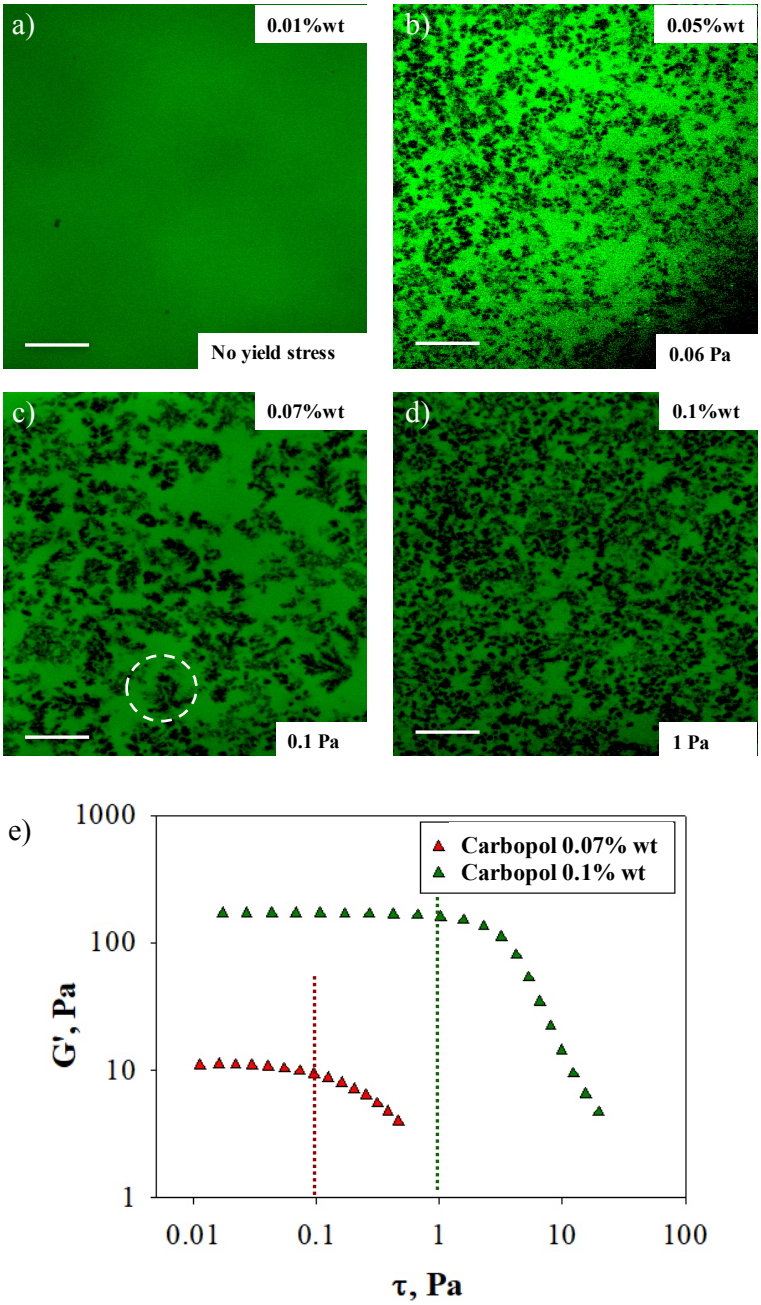

Figure 6: Confocal images at different Carbopol concentrations at same neutral pH (6-7). The scale bar corresponds to 10 μm. Values of static yield stress at each concentration are shown at the bottom right of the images and have been estimated by G' vs τ, as reported in e). The dashed circle in c) highlights a dendritic-like structure. e) G' as a function of shear stress τ for 0.07% wt (red triangles) and 0.1% wt (green triangles) at the frequency of 1 Hz. The yield point has been estimated by taking the initial drop of G′

The black spots can be identified with Carbopol particles, since, due to steric hindrance, FITC cannot access the water inside them, so that only the aqueous suspending phase is bright and is displayed in green color in the figures. The dyed sample was stored in a refrigerator at 4° C and it was stable over a week.

By using image analysis, it is found that the dispersed phase made by the Carbopol particles occupy a fraction of the image area much larger than the percent Carbopol concentration, even upon accounting for the different density of water and polyacrylic acid (the polymer chains have a density of 176 Kg/m^3, while for the gel suspension a density comparable to water was measured) and the depth of field of the 100x objective (about 0.7 μm). This finding supports the initial hypothesis that Carbopol particles are highly swollen, in agreement with previous literature results showing that polyacrylic acid particles in water tend to a remarkable swelling [30, 39] after neutralization.

6 Thermodynamic analysis of Carbopol

6.1 Imaging as a quantitative method to understand Carbopol swelling

Altogether, the previous observations can be interpreted in terms of a two-phase microstructure made of a continuous water phase (labeled with FITC) and a dispersed polymeric micro-gel (black)[68]. To elucidate this point, in Figure 7a experimental data of Carbopol weight concentration are plotted as a function of the volume fraction of Carbopol particles (measured as the fraction of the image area taken by particles).

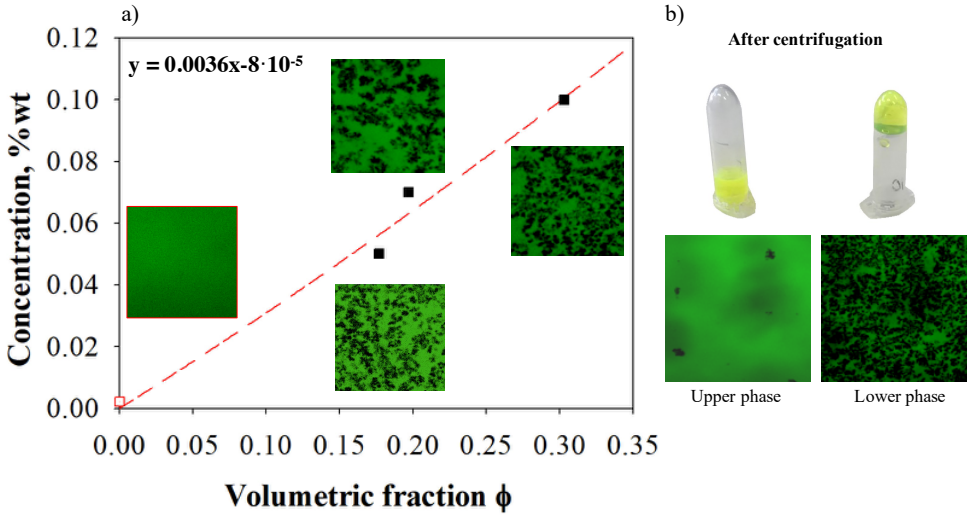

Figure 7: a) Plot of Carbopol weight concentration as a function of particle volume fraction; b) photographs of the test tubes after centrifugation. Confocal microscopy images of upper and lower phases after centrifugation are also shown

The data are well represented by a linear regression, indicating that there is a linear correspondence between the two quantities. The 0.01% wt concentration (red dot), corresponding to a homogenous sample with no Carbopol particles, was not considered for calculating the linear regression, as it will be explained later.

By image analysis and by using the linear regression as a calibration line, the swelling ratio, defined as the mass of swollen Carbopol particles to the dry mass of the Carbopol added during preparation, was obtained. The swelling ratio was calculated as the ratio (mass of swollen polymer)/(mass of dry polymer). The swollen polymer is given by the black particles, which, due to the small Carbopol concentration, can be taken as essentially made of water. So, the mass of swollen polymer is equal to the volume fraction of black particles multiplied by water density (1 g/ml). The mass of dry polymer can be obtained from the weight concentration. The calculation was made on a basis of 100 g of Carbopol suspension (corresponding to a volume of 100 ml). For example, at 0.07% wt Carbopol concentration the volume fraction of Carbopol particles is equal to 20% from Figure 7, giving a swelling ratio of

$$\frac{20}{0.07} = 285$$

Such high values of the Carbopol swelling ratio have also been found before [69].

This behavior is typical of microgel systems where particles are swelled by the presence of water due to osmotic phenomena [30, 39, 70]. In fact, NaOH addition leads to an osmotic pressure caused by ion exchange between the polyelectrolyte particles and solution. Such imbalance drives water flow in Carbopol particles, thus swelling them and inducing a two-phase microstructure.

6.2 Carbopol as miscible gap system description

To separate the two phases for further characterization, a series of centrifugations was carried out. As shown in Figure 7b, after repeated centrifugations (described more in detail in the Materials and methods section), two phases could be clearly distinguished by turning the centrifugation vial upside down: a low viscosity upper phase, which flowed down the vial (Figure 7b left side), and a lower phase, which remained stuck at the bottom of the vial (Figure 7b right side), thus suggesting a strong yield stress character. The confocal microscopy images of the two separated phases in Figure 7b show that almost all the Carbopol particles migrated in the lower phase showing that a dense dendritic-like microstructure has been formed. The two phases separated by extensive centrifugation were also characterized by rheological tests. Before centrifugation, viscosity measurements show a shear thinning behavior (Figure 8, hexagons), typical of yield stress solutions, with the

shear stress increasing as a function of shear rate over the entire range investigated. In particular, data at 0.1% wt are well described by the fit proposed by Dinkgreve et al. [59] for yield-stress fluids (data not shown for the sake of brevity). On the other hand, the upper phase of the centrifuged sample shows a nearly constant viscosity (squares) close to the value of water viscosity (dotted line), independent on Carbopol concentration. The small difference with respect to water (about 5%) and the slight shear thinning at low shear rates can be attributed to the Carbopol polymer molecules dissolved in the continuous phase.

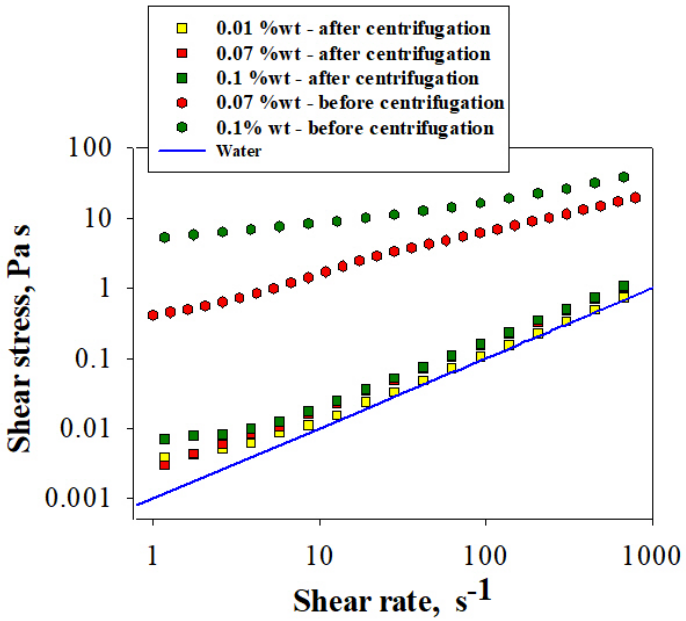

Figure 8: Viscosity measurements, reported as shear stress as a function of shear rate, before (hexagons) and after (squares) centrifugation. The latter are referred to the upper phase. Solid blue line corresponds to water viscosity

This result provides further evidence that the microstructure of Carbopol in water at the polymer concentrations 0.05, 0.07 and 0.1% wt corresponds to two equilibrium phases, a dispersed one made by swollen Carbopol particles, and the continuous one made essentially by water. The fact that the continuous water-rich phase has a viscosity independent on Carbopol concentration provides evidence that the continuous phase has a constant composition in the concentration range investigated.

6.3 Isothermal phase behavior using microscopy and mass balance

If one combines this result with the linear trend of Fig. 7a, it can be concluded that both phases have the same composition independent on Carbopol concentration. Indeed, by making a material balance on a unit total mass basis (e.g., 1 g)

$$1 = L' + L"$$

$$z = L'x' + L"x"$$

where *L'* and *L"* are the mass fractions of the dispersed and continuous phase, *z* is the total Carbopol concentration, and *x'* and *x"* are weight concentration of Carbopol in the two phases. By combining the above two material balances and

recognizing that mass fractions are in fact coincident with volume fractions (given the low Carbopol concentrations), one gets the equation:

$$z = x'' + (x' - x'')\phi$$

where $\phi \equiv L'$ is the volume fraction of the dispersed phase. Hence, the two variables of the plot in Fig. 7a (i.e., z and ϕ) are linearly related provided that *x'* and *x''* are constant, independent on Carbopol concentration. This behavior is typical of the two equilibrium phases of a binary miscibility gap [71] and has been found in other polyelectrolyte solutions [72]. The three samples within the miscibility gap (0.05, 0.07 and 0.1%) differ among each other only for the relative amount of the two phases (but not for their composition), with an increasing volume fraction of the particle dispersed phase at increasing Carbopol concentration. From the linear fit in Figure 8a, the compositions of the two phases should be 0.008% (which is quite close to the 0.01% concentration where no Carbopol particles are observed and was therefore not included in the linear fit) and 0.36%.

The particles in the dispersed phase tend to aggregate (see images in Figure 6), and this behavior could be of entropic origin, since the Carbopol polymer

molecules in the continuous phase may generate depletion attractions between the particles [1, 73]. Particle aggregation can be related to the yield stress of Carbopol solution [25], which is a topic quite investigated in the literature, but not fully elucidated yet. The onset of yield stress behavior can be interpreted as the formation of a network of aggregates spanning the entire system (percolation), such as in gelled systems [74]. The limiting volume fraction where a non-zero yield stress was measured (see Figure 7a), which is 0.15 (corresponding to a Carbopol concentration of 0.05%), is close to the critical volume fraction of spherical attractive particles for percolation [75]. The presence of dendritic-like structures in Figure 1 (see the dashed circle in Figure 6c) is likely to contribute to the percolation of the Carbopol microstructure. This was a starting point for a work that is still under development that it has as target the building of the phase diagram of Carbopol as a function of temperature.

7 Temperature effect on Carbopol - Phase Diagram

Due to verify the hypothesis that Carbopol water solutions behaves as a miscible gap system, a series of experiments as a function of temperature has been performed. The target of this campaign was to build the phase diagram combining microscopy and rheology.

Firstly, a calibration line correlating the apparent viscosity as function of concentration was built. The concentration investigated have been chosen in a range of dilution where this correlation is linear and the viscosity was measured using a capillary rheometer (Ubbelohlde with a radius of R=50 μm).

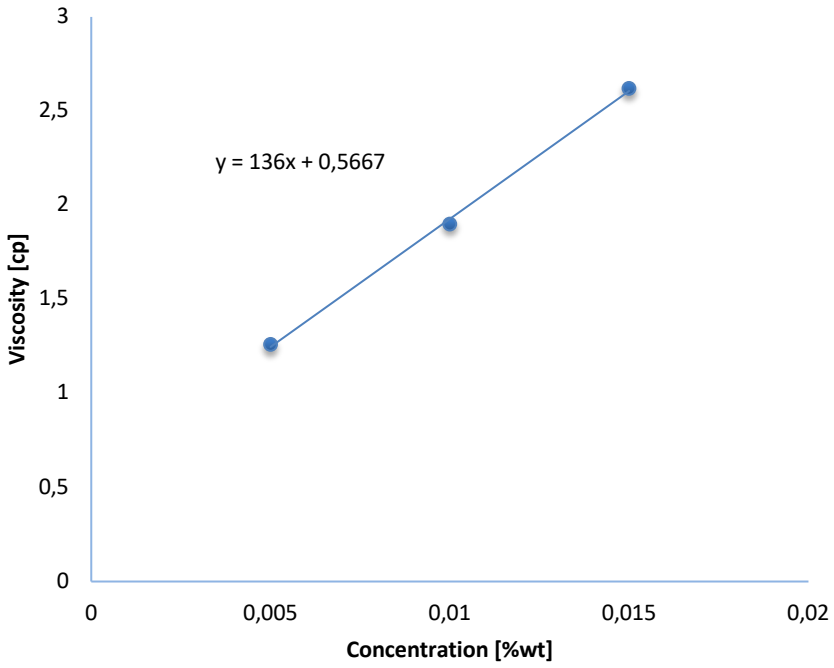

Figure 8: Viscosity as a function of Carbopol concentration

This correlation was used to calculate the concentration of the continuous phase obtained performing centrifugation at a fixed temperature. Knowing the concentration x' and calculating the volume fraction of the particles using the technique previously shown, it is possible to calculate also the concentration x'' of the dispersed phase.

In fact, using the equation:

$$z = x'' + (x' - x'')\phi$$

Is possible to calculate knowing the volume fraction from imaging, for each pair (z, x') the relative x'' building the following table.

Temperature [°C]	X' **[%wt]**	X'' **[%wt]**
10	0.0055	0.242
20	0.008	0.217
30	0.0125	0.195
40	0.0218	0.165

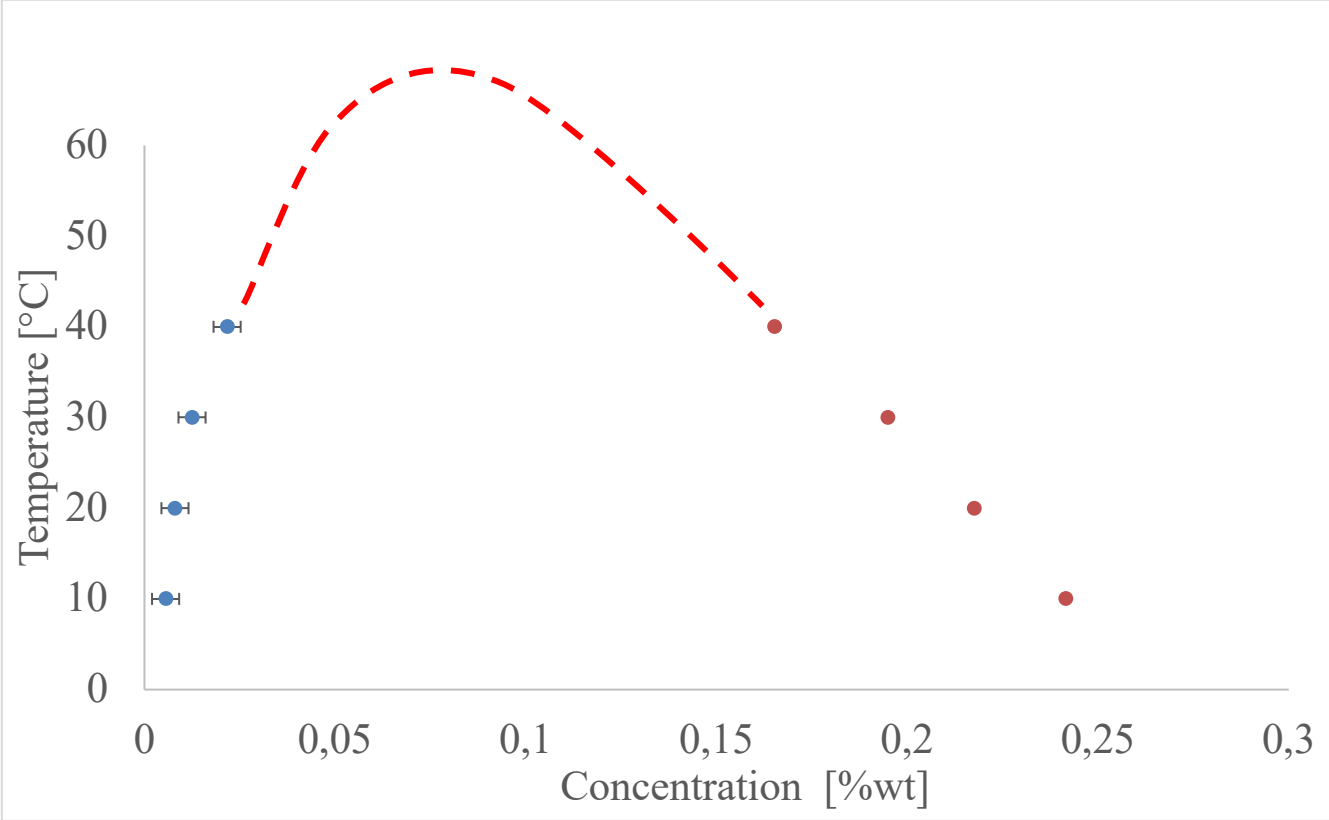

Figure 9: Phase diagram of Carbopol- the blue dots are the experimental data while the red line is an extrapolation based on single experimental investigation. The orange dots are calculated from the mass balance

The upper graph combines the experimental results obtained with a plausible extrapolation of the diagram obtained. To confirm our hypothesis two different experiments were carried out. Firstly, a sample at concentration of Carbopol around 0.07% wt was heated at a temperature of 70° C, a condition presumably outside of the gap, and then cooled down to get inside the diagram along a vertical line.

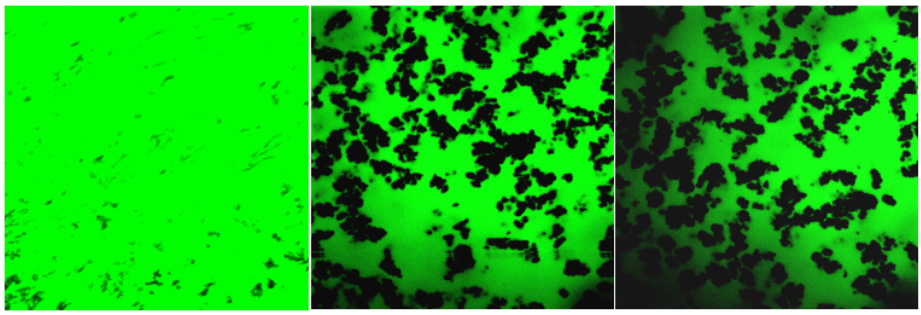

Figure 10: Time evolution of Carbopol 0.07% wt in a cooling down process from 70° to 25°

What is possible to observe that the intensity of the sample in the first instant is much stronger and the Carbopol particles are almost completely dissolved in the matrix. After few instants the system starts to separate in two different phases independent one from each other confirming that we are transitioning from a homogenous sol phase to a biphasic gel.

This result is in agreement with classic model for associative polymers [72] were starting from Flory theory theoretical diagrams are built. Furthermore, it was analyzed also a concentration of 0.3% wt that corresponds to a point on the diagram outside the gap on the right side.

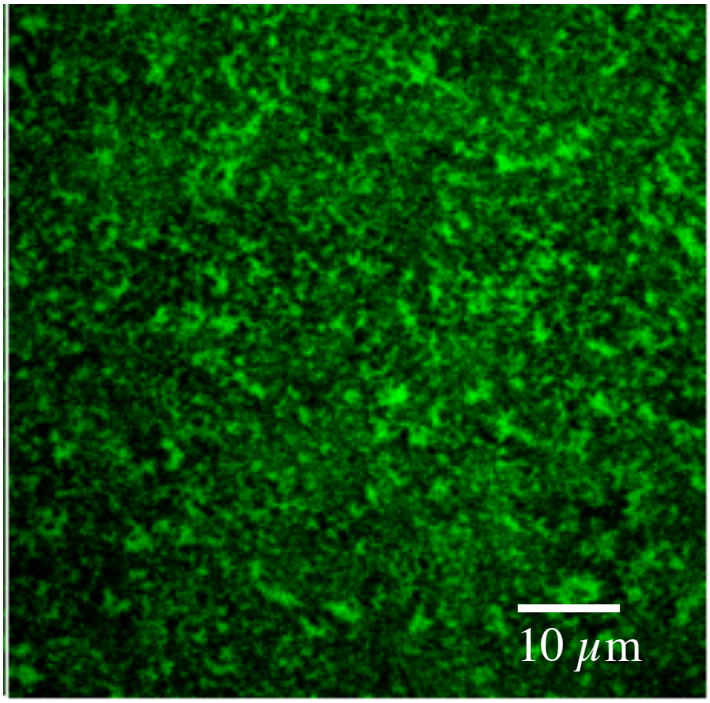

Figure 11: Carbopol 0.3% wt at 30°C - gel system

In this part of the diagram the system is a gel and using imaging is not possible to distinguish two isolated phases (black particles dot on a green background) but the system is more homogenous on a dark green scale, due to the penetration of water + FICT inside the particles that are extremely swelled. There are some green spot that can be explained considering that the jamming happened leaving a porosity in the system as happens for other systems like gelatin.[76]

This study is still in progress and it will be part of a future paper. While the previous and following results on Carbopol have been published on Journal of Colloid and Interface Science [68].

8 Flow behavior and microstructure of Carbopol suspensions in tubes

While Carbopol based systems have been widely studied in static conditions and by rheological measurements, only few reports are present in the literature about their flow behavior in tubes. Carbopol suspensions under flow have been investigated [12, 77, 78] by PIV (Particle Image Velocimetry) in mm-sized tubing, and velocity profiles with an extended plug core at the centerline, typical of yield stress fluids, was found. Here, microfluidics coupled with high-speed microscopy was exploited to investigate the velocity profile under confined flow conditions. In particular, Carbopol aqueous suspensions were fed to a micron-sized glass capillary (ID 320 μm), and 4 μm polystyrene micro-particles dispersed in the suspensions were used as tracers. In Figure 12a, the velocity profile (red circles) at ΔP=400 mbar is reported, showing the typical plug core due to yield stress and the velocity drop away from capillary centerline. The composite image (obtained by combining the images of sequence into a single, maximum contrast image, see Materials and Methods) is also reported (Figure 12c).

The composite image shows a tracer-free layer, about 20 μm wide, close to the capillary wall (see red dotted lines in Figure 12a).

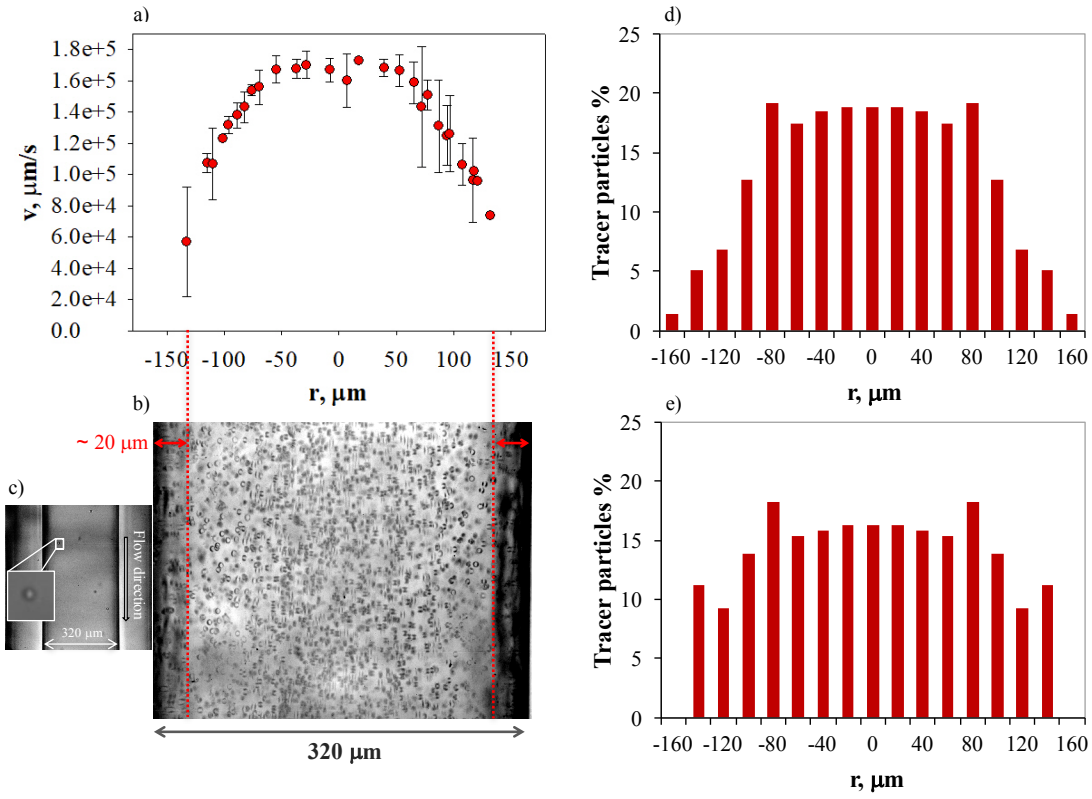

Figure 12: a) Plot of velocity (left y-axis) and mean grey level (right y-axis) as a function of radial position, b) image of the capillary with the inset showing a zoomed view of a polystyrene particle, c) composite image of the capillary obtained by combining all the images, like the one in b), in a video recording. d) Radial distribution of tracers. e) Radial distribution of tracers normalized with respect to their velocities. ΔP=400 mbar, Carbopol concentration = 0.07% wt

To quantify the radial distribution of the tracers, the center plane of the capillary was divided in 32 layers, each accounting for 10 µm. To improve the statistics, the number of tracer particles was averaged between pairs of layers symmetric to the centerline [79]. By plotting the percentage of tracers per layer as a function of capillary radius (Figure 12d) a simil-parabolic distribution with a central plug core was found, resembling the velocity profile (Figure 12a). This distribution could be explained due to the fact that the number of travers traveling across the field of

view in a given time interval was higher in the center of the capillary than near the wall due to the different velocity. In fact, by normalizing with respect to the number of tracers in each layer with the corresponding velocity, the distribution is more uniform (Figure 12e), with a little decrease in the central zone, likely due to the presence of Carbopol aggregates. These results are in line with previous results obtained in the case of micron-sized drug carriers flowing in the presence of red blood cells in microcirculation [80].

Hence, the velocity profile could be measured only up to a radial position of ~140 μm, because no tracer particles were found closer to the capillary wall. In the literature, the presence of a near-wall region with a strong velocity gradient in Carbopol fluids has been ascribed to a wall slip phenomenon arising from flow-induced structuring and leading to local properties quite different with respect to the ones of the core region [81, 82].

In this work, flow velocimetry was complemented with confocal microscopy in the same microfluidic set-up[68], with the purpose of correlating flow-induced microstructure and velocity profile. As shown in Figure 13, three regions along capillary radius can be distinguished by looking at particle concentration: i) a central core, characterized by a high concentration plug with Carbopol particles travelling at the same velocity, which can be related to the yield stress; ii) an

intermediate layer, where Carbopol particle concentration is lower, corresponding to the drop of velocity in the profile of Figure 12a; iii) a near-wall region, where Carbopol particles accumulate, likely due to shear-induced diffusion. In fact, under confined conditions, micro-sized particles are pushed away from the capillary wall by a wall-induced lift, but this effect is counterbalanced by the shear-induced diffusion of smaller particles that arises due to particle-particle collisions. This leads to the migration of the larger Carbopol particles towards capillary centerline, creating a concentrated core in the center, and the diffusion of smaller particles towards capillary wall, in analogy with the margination of platelets in human microcirculation [80] and with the radial distribution of droplets in confined tube flow [83].

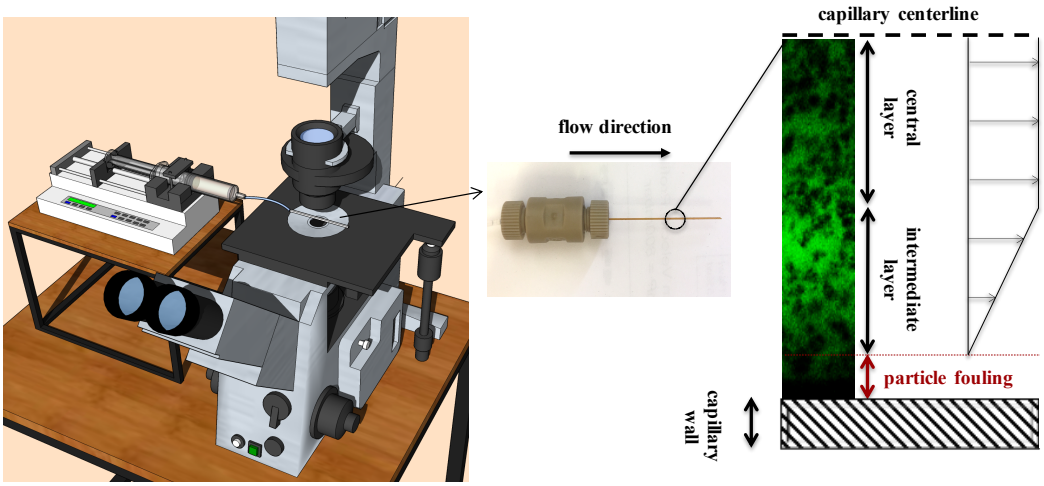

Figure 13: Experimental setup on the left side and confocal image of a Carbopol suspensions flowing into the 320 μm ID capillary. Only half capillary is shown for clarity

The observed particle accumulation is reminiscent of the fouling process, whereby particulate or molecular aggregates adhere and grow onto a surface or a membrane, eventually leading to channel clogging [84]. Particle aggregation can be enhanced by the applied flow, since the frequency of particle-particle collision is an increasing function of shear rate [85]. Aggregate size and shape is strongly dependent on surface chemistry and shear flow [86], with more compact aggregates corresponding to higher shear rates, until a critical value is reached beyond which aggregates detach from the wall [85, 87]. However, we do not observe any growth or break-up of the fouling layer in the time frame investigated (i.e., less than an hour), and this could be explained by the fact that the accumulation of Carbopol particles on the capillary wall occurs at the beginning of the experiment, during capillary filling, likely due to chemical interactions between Carbopol and capillary surface. A similar behavior was found in the deposition of salts on the walls of a microfluid channel served a similar behavior in the deposition of salts on the walls of a microfluid channel [84, 85].

Here, by using confocal microscopy we show the presence of a Carbopol concentrated near-wall layer, due to a fouling-like process, where tracer particles are entrapped and cannot flow. The adjacent layer is also devoid of tracers and can

be likely ascribed to wall slip, commonly found in suspensions [88-91]. Similar results were obtained at different ΔP (200, 600, 800 mbar) and capillary diameter (180 μm), but are not reported for the sake of brevity. Confocal microscopy under flow allowed also to show that the core region is characterized by high Carbopol particle concentration (volume fraction about 80%), corresponding to a plug structure, whereas the intermediate layer corresponds to lower concentrations (volume fraction about 20%), hence to lower viscosities (the values were obtained by the same approach used above for the calibration line). The presence of a layered microstructure is also found in confined shear flow of other complex fluids, such as emulsions [83, 92], blood [80] and surfactant suspensions [64].

The flow-induced microstructure with two layers having different rheological properties corresponds to the general picture underlying models such as Bingham and Herschel-Bulkey [1], which describe in a qualitative or semi-quantitative way yield stress fluids. By making a shear stress balance, the following equation to calculate the yield stress can be obtained:

$$\tau_0 = \Delta P/L * r_0/2$$

where r_0 is the radius of the central plug region and can be estimated from image analysis. In this way, a value of $\tau_0 = 20$ Pa can be obtained from the data of Figure

12a. Such value is much larger than the one (i.e., 0.1 Pa) shown in Figure 6 for the same (0.07% wt) Carbopol concentration. Based on the confocal images of Figure 6 and 7 the discrepancy can be attributed to the different microstructure of the Carbopol suspensions in the two experiments, i.e. for free *vs* confined Carbopol suspension. While the yield stress measured by classical rheometry can be related to the presence of a particle network spanning the entire suspension volume, the yield stress obtained from the velocity profile is due to the heterogeneous particle distribution along the capillary radius.

9 NMR- Novel technique to investigate flow of yield stress liquids in real porous media

NMR-Mouse used in the context of porous media and Newtonian liquid adsorption is a technique well established. A better understanding of the functionality of materials in the context of fluid distribution and dynamics, it has been studied in the latest years [65, 93].

An evolution of this approach will be to go in the context of Non-Newtonian fluids. Quantitative experiments of Carbopol liquid distribution in porous media have been performed in collaboration with Dennis Woertge, PhD student from the

University of Ilmenau, Germany in the Procter and Gamble German Innovation Centre.

To achieve this goal, previous calibration was needed to correlate the signal coming from the instrument that is in arbitrary unit to the volume of liquid, as shown in the Figure 14. A fixed volume of Carbopol was added to a glass slide positioned on the instrument and the signal was recorded as a function of distance from the magnet of the instrument.

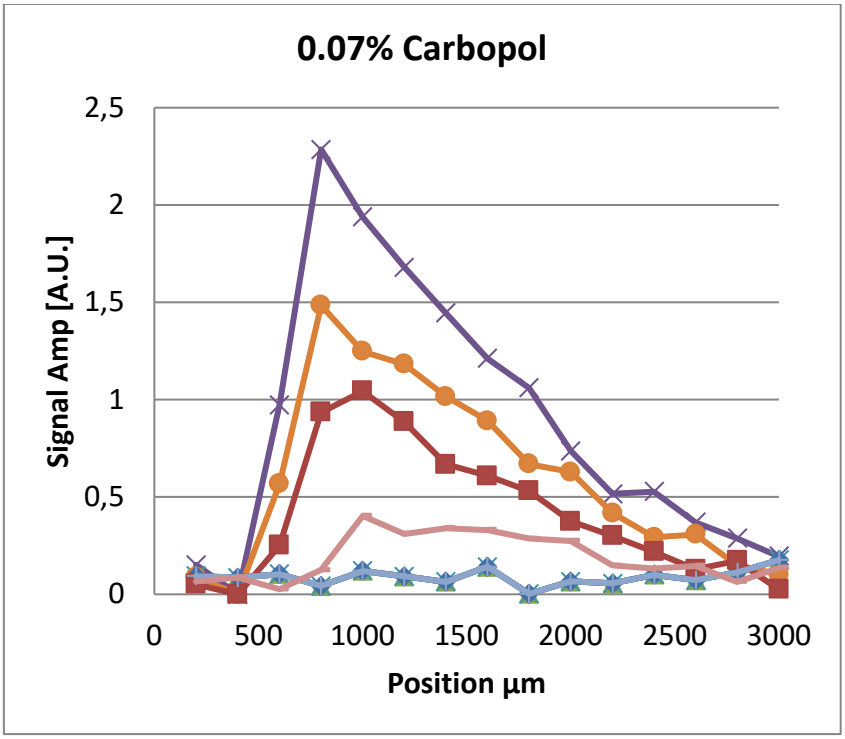

Figure 13: Calibration NMR signal-volume in µL of Carbopol

First, 100 μL were added to the glass slide and later the same system was scanned increasing the volume, up to 400 μL. Calculating the area under the curve shown in the Figure 13 and plotting it as a function of the volume, we found a linear trend confirming the possibility to be quantitative with these liquids. These linear trends have been compared in Figure 14, changing the concentration of Carbopol. We can observe that the 0.07% wt and 0.1% wt concentrations present the same slope, and this result can be explained in terms of relaxation time of the protons in the system. Carbopol at 0,07% wt and 0,1% wt is still under its jamming point and this results in the same T_1 relaxation times, while the sample at 0,5% wt is already a gel with a slightly shorter T_1, showing a different slope in the calibration line.

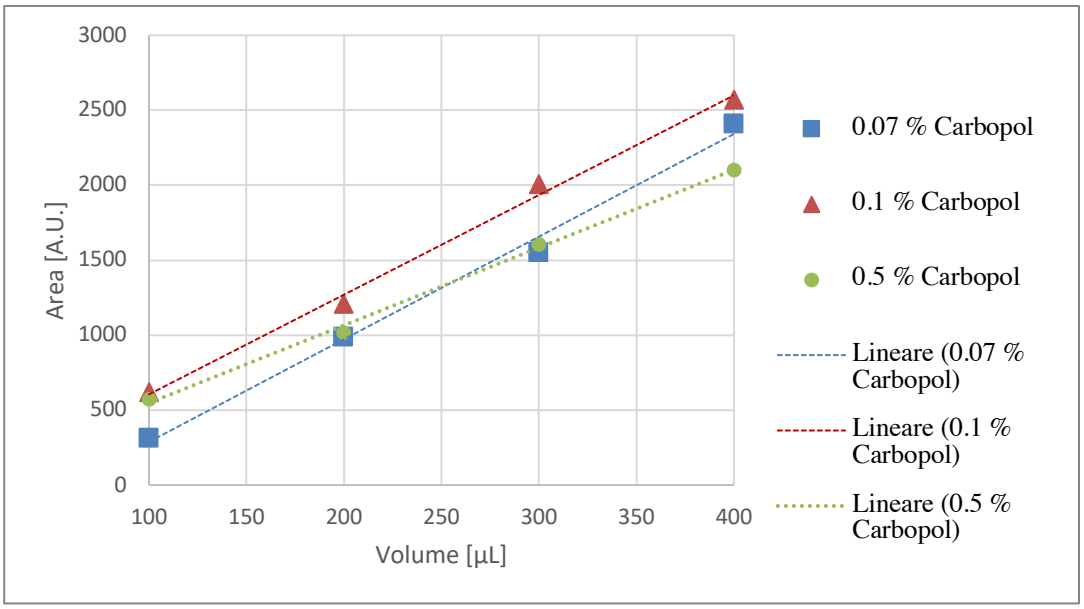

Figure 14: Area of the peak as a function of volume for different Carbopol concentration %wt

These results will allow future studies of the flow performance of Carbopol gels in different porous media as a function of yield stress.

A first investigation was realized during my period abroad at the German Innovation Centre of Procter and Gamble.

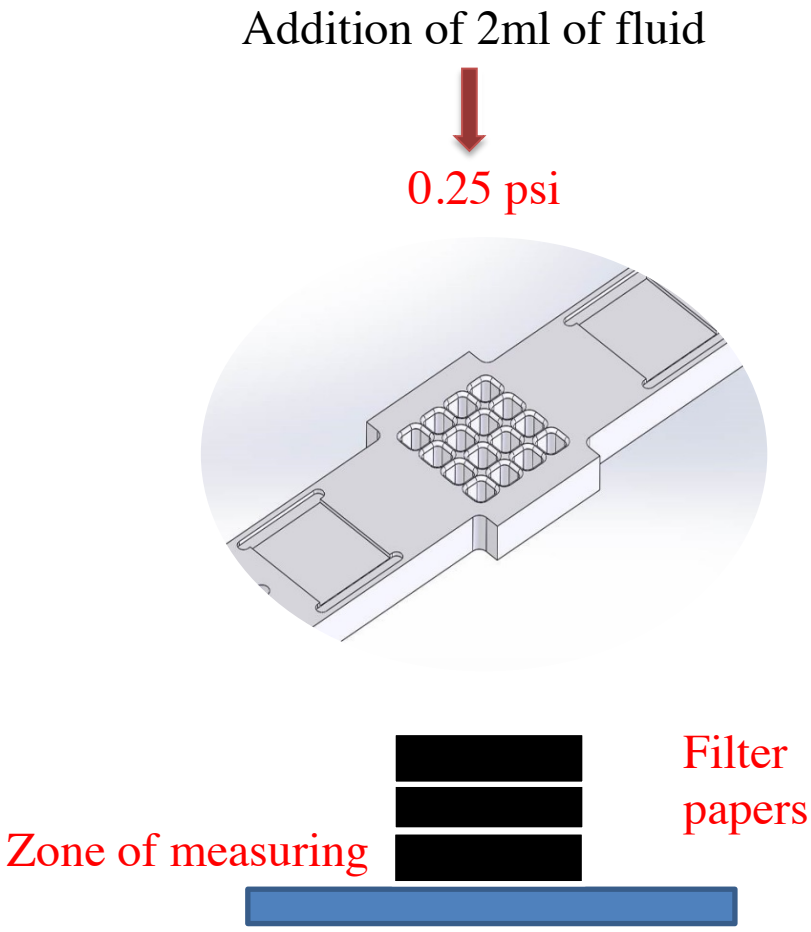

Figure 15: Experimental set-up

A model system made up of three layers of filter paper cut in 4x4 cm square was used as a porous medium. The experimental setup is shown in Figure 15. A volume of 1mL of liquid it has been applied on the first layer using a syringe pump and the kinetics of drainage was studied in the bottom layer as reported in Figure 16.

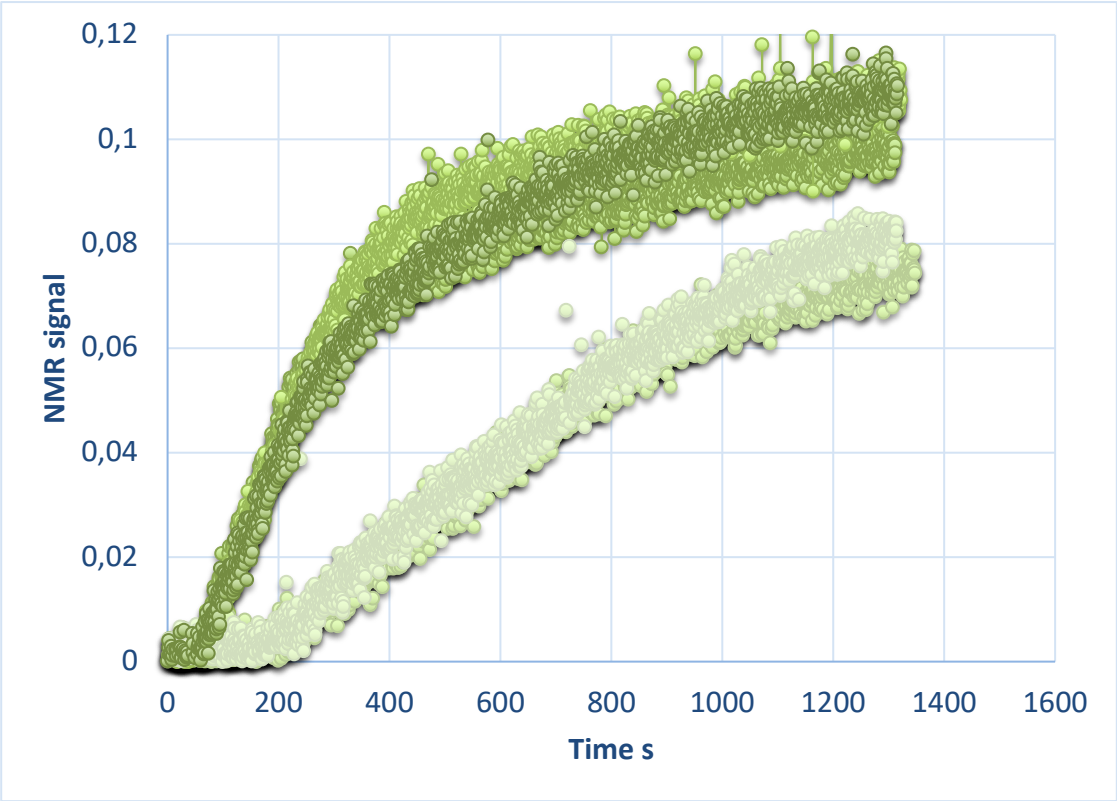

Figure 16: NMR signal in FP as a function of time for Carbopol 0.07%wt (dark green) and 0.1%wt (light green)-the overlap of multiple curves enable to verify the reproducibility of the technique

The sensitivity volume was fixed in the position of the bottom layer, so it takes some time from the liquid application to visualize some signal in filter paper. It can be noticed that lower concentration (lower yield stress) reached faster the bottom part of the media and with a higher amount of liquid, as said before about the signal amplitude. Furthermore, a yield stress ten times higher in the Carbopol generates a delay time in the start of the flow. In fact, the liquid takes several minutes to reach the filter paper at higher yield stress. At the end of the experiment, a profile of the signal along the whole sample was taken (Figure 17).

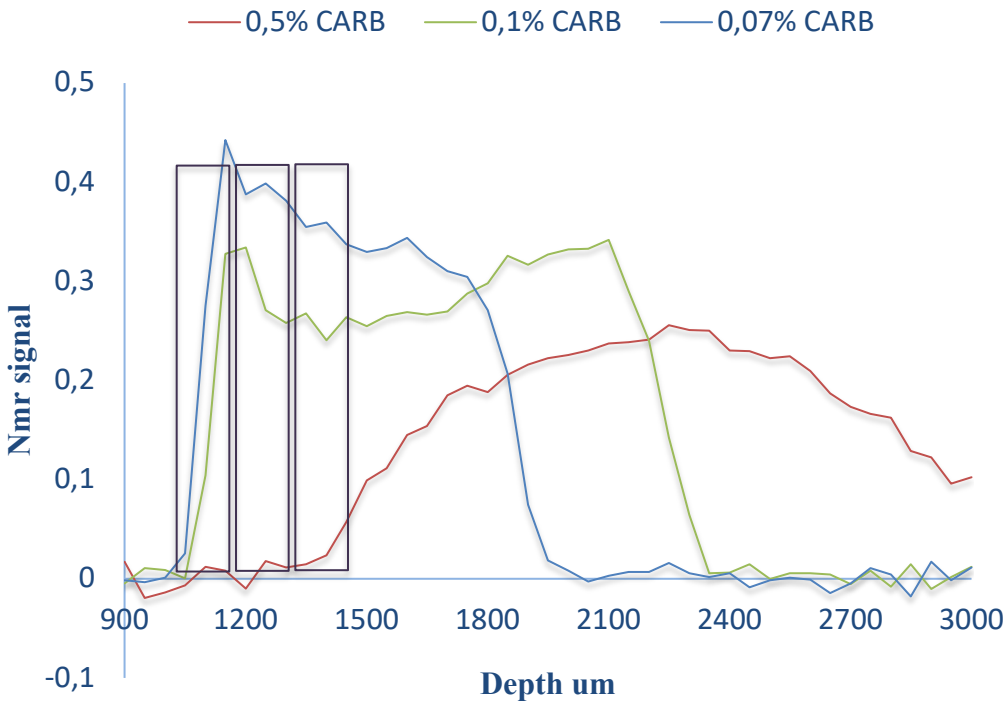

Figure 17: Equilibrium liquid distribution in PM

Since the area under the curve is proportional to the volume of liquid inside the system, it can be observed that the liquid distribution depends on Carbopol concentration. In fact, lower is the yield stress, higher is the amount of liquid that reaches the bottom layer. For the highest concentration (0,5%wt) the yield stress does not allow the drainage of the liquid at all. Most of the signal coming from the liquid is outside the filter paper layers and so it is given by the droplet of liquid that is still on the surface of the top sheet. This result is incredibly interesting since

it means that the capillary force is not strong enough to allow the complete adsorption.

In future collaborations, woven materials will be used with a fixed mesh and the signal will be converted in volume using the calibration previously shown.

10 An Alternative Approach for Measuring Yield Stress in Carbopol Microgel

A novel experimental apparatus for the direct measurement of yield stress was conceived and realized in collaboration with the Professor Lanotte group at the Department of Physics of the University Federico II. It is based on a torsion pendulum equipped with a magnetic dipole and a rotating cylinder immersed in the material to be investigated. The pendulum equilibrium state depends on the mechanical torque applied due to an external magnetic induction field, elastic reaction of the suspension wire and shear yield stress. Experimental results were reported showing that the behavior of the pendulum rotation angle, in different equilibrium conditions, provides evidence of the yield stress presence and enables its evaluation by equilibrium equations. The dependence on time of the equilibrium approach was also studied, contributing to shed light on the relaxation

effect in the transition from a fluid-like to solid-like behavior, as well as on the eventual thixotropic effects in non-Newtonian fluids. As test fluid Carbopol solutions with different weight percentages were chosen. The linear procedure, combined with the effectiveness and reliability of the proposed experimental method, candidate it to be used for the study of peculiar behaviors of other yield stress complex fluid such as blood, crude waxy oils, ice slurries, coating layer used in food industry and also for fault sliding in geodynamics.

10.1 Experimental apparatus and theory of the measure

The figure below shows a schematic of the experimental apparatus designed to measure yield stress of a complex fluid. A nylon thread, stretched along the vertical axis (Y), constitutes a torsional pendulum together with the magnetic dipole, which has a moment μ (78 mA m^2), and the inert plastic cylinder (I C), both tied, balanced and coaxial with the wire itself. Using the standard calibration curve of the elastic reaction torque for the used wire, the value of the elastic torsion constant K = $131 \cdot 10^{-7}$ Nm was easily determined. The external cylinder (E C) is fixed to the ground. The radii of the inner and outer cylinders are R_1= 7.0mm and R_2= 15.0mm respectively. The yield stress fluid (YSF) to investigate is transferred, taking it with pipettes from the container in which it has degassed, and slowly introducing it into the cavity between the two cylinders, accurately avoiding the

formation of air bubbles. This operation was continued until the inner rotating cylinder is immersed in the sample for a height h. We underline that the rotating cylinder is perfectly balanced and solidly bound with respect to the suspension axis, which is also the rotation axis, and any vertical thrust (Archimedes thrust, elastic reaction thrust that tends to make the cylinder float) are balanced by the tensile stress in the suspension wire.

The magnetoelastic resonator (M R), whose signal is processed by a Signal Analyzer (S A), has a core consisting of an innovative nanocrystalline material. This soft ferromagnetic core is high sensitive to changes in the local magnetic field [94]. When the pendulum rotates, the magnetic dipole, rigidly connected to it, also rotates inducing a decrease in the magnetic field component coaxial with the sensor.

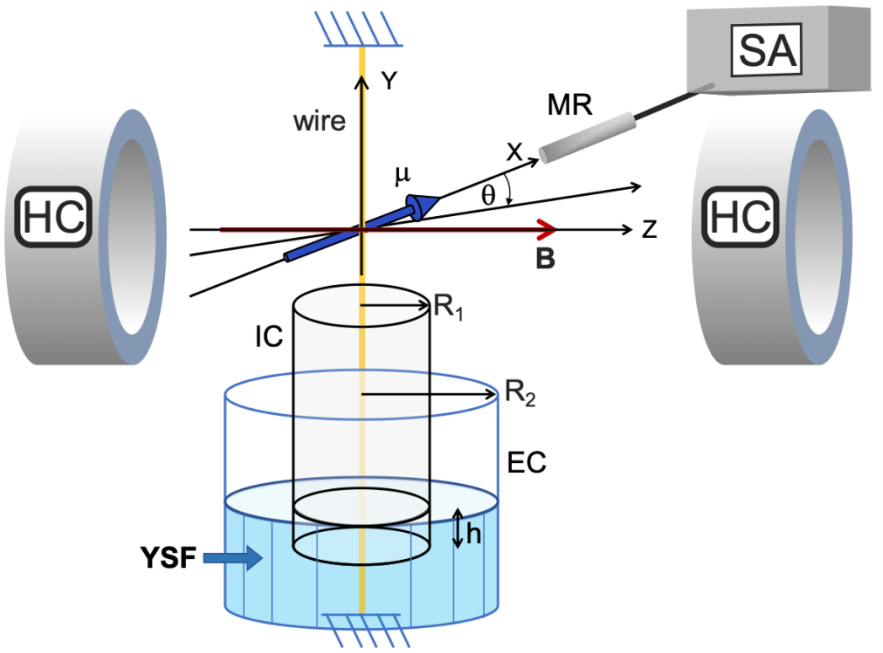

Figure 18: Scheme of the prototype experimental apparatus: symbols as described in the text

Therefore, any rotation (θ) of the pendulum around the Y axis is detected with high sensitivity (±0.25°). This methodology has been explained in detail in reference [95]. In that previous investigation, the damped oscillation of a similar torsional pendulum, immersed in a fluid, were studied to determine the material viscosity. In this case, instead, the measurement technique is fundamentally different since it consists of determining the condition of static equilibrium of the pendulum. Moreover, important components were added to the original apparatus. In particular, a standard system of Helmholtz Coils (HC) was integrated for applying a static magnetic induction field B along the Z axis, which is perfectly

orthogonal the suspension wire, on Y axis, and to the magnetic dipole in the rest position (Figure 18). Both the rotation stimulation and the equilibrium position are determined by the torque produced by the field B. The rotation angle is also directly visualized using a standard protractor, that is fixed in the horizontal XZ plane and coaxial with the Y axis. The MR sensor is not influenced by magnetic induction field B since it is sensitive only to magnetic component along X axis. The external EC ampoule is immersed in a thermal bed, maintaining a constant temperature (20 °C) by means of a thermostatic set up [95]. Figure 19a shows an image of the experimental equipment (snapshot from above).

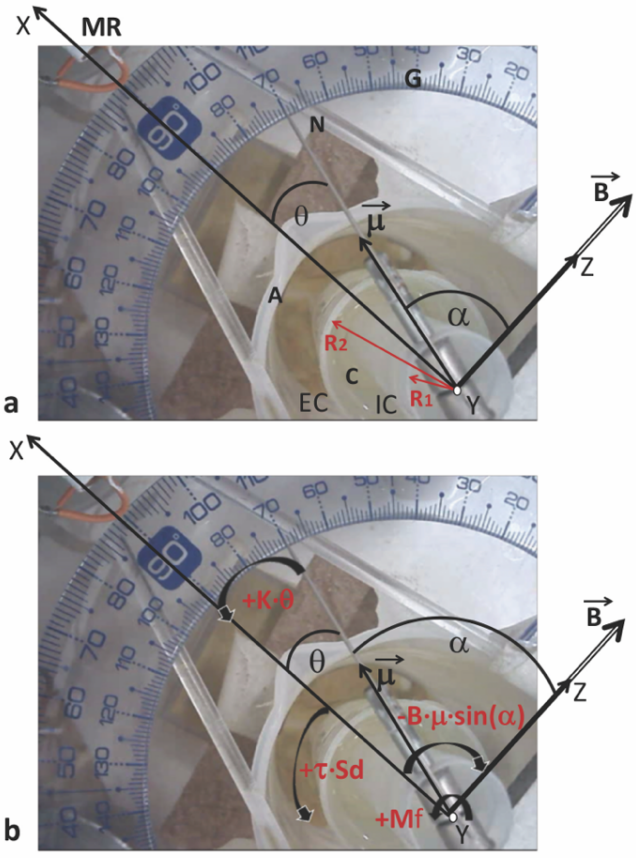

Figure 19: **a**. Photography of the experimental apparatus showing the torsional pendulum system -suspension wire along Y axis + rotating magnetic dipole in the plane XZ + empty cylinder (IC)-, the external cylinder (EC), the yield stress fluid (C) which fills the cylindrical crown to a controlled level, the external ampoule (A) in which water is kept at constant temperature, the needle (N) glued to the magnetic dipole, the protractor fixed on the XZ plane and centered on the Y axis, the position of the magnetoelastic resonator (MR) for the precise measurement of the rotation angle. **b**. Scheme of the scalar components of the mechanical moments along Y axis in any equilibrium condition reached after the application of a magnetic induction field directed along Z axis. The figure shows the sign of Y scalar components of the magnetic torque (- μ B sin(α)), the mechanical reaction torque (+Kθ), the yield stress torque (+τ S_d), and the internal friction torque (+Mf) in the case examined, i.e. when equilibrium is achieved through clockwise rotation.

It is possible to see the permanent magnet, that constitutes the magnetic dipole μ, the internal and external cylinders (IC and EC respectively) and the Carbopol solution (C) between them. A nonmagnetic stainless-steel needle is also visible, integrated with the

pendulum system and coaxial with the magnetic dipole. This needle is a guide for visualizing the rotation on a protractor (G in Figure 19a), fixed on a horizontal plane and centered on the Y axis, along which the nylon suspension wire is stretched.

In the case shown in Figure 19, the applied field $B \neq 0$ produces the reduction of the α angle between **B** and $\boldsymbol{\mu}$ from the initial 90°, in the condition of B=0, to the final 70°. Since α is complementary to the rotation angle, the latter assumes the value $\theta = (\pi/2 - \alpha) = 20°$. In fact, when a magnetic induction field is applied, the torsion pendulum is subjected to a magnetic torque $\boldsymbol{\mu} \wedge \mathbf{B}$, whose modulus is $\mu \cdot B \cdot \sin(\alpha)$ inducing a clockwise rotation around Y (see Figure 19b).

On the other side, starting from the position in which the pendulum is not subject to any external stimulus, when a rotation of θ intensity is produced, a mechanical reaction torque of modulus $K \cdot \theta$ - and direction indicated in Figure 19b- is also applied to the pendulum, being K the elastic torsional constant of the suspending wire. Moreover, when a static equilibrium is established, if there is a fluid between the internal and external cylinder, a mechanical moment also acts due to the shear yield stress (τ_y) applied by the fluid on the cylinder surface ($\tau_y \cdot S_d$ Fig. 19b). This mechanical moment is than applied on the cylinder surface immersed in the solution (base area ΠR_1^2 and eight h, Figure 1) by the fluid which is in contact with this surface in static condition: the fluid not in contact with the cylinder does not apply any action on it. In the described experimental conditions, the intensity of this torque can be expressed as $\tau_y \cdot S_d$, where τ_y is the constant yield stress and $S_d = \int_S r \cdot$

dS, where S is the surface of IC wet by the fluid and r is the distance of any elementary surface dS from the rotation axis Y. In the investigated case, it results in

$$S_d = 2\pi {R_1}^2 h + \int_0^{R_1} 2\pi r^2 dr \qquad (1)$$

Since R_1=7 mm and h=3mm or h=9mm were used in the experimental apparatus, the values S_d= $1.6 \cdot 10^{-6}$ m^3 or $3.5 \cdot 10^{-6}$ m^3 are obtained respectively.

Ultimately, whenever the pendulum stops in static equilibrium at an angle θ_e, the sum of all the components along Y axis of the applied torques must be equal to zero. Therefore, referring to the scheme in Figure 2b, the following equation can be applied:

$$-B\mu \sin\left(\frac{\pi}{2} - \theta_e\right) + K\theta_e + \tau_y \cdot S_d + M_f = 0 \qquad (2)$$

where, summarizing for the sake of clarity, $\tau_y \cdot S_d$ is the torque due to the shear yield stress in the points of the static fluid in contact with cylinder IC (Figure 1), $-B\mu \sin\left(\frac{\pi}{2} - \theta_e\right)$ is the torque component applied by the external magnetic field in consequence of the presence of the magnetic dipole glued to the pendular system, $K\theta_e$ is the torque component due to elastic torsional reaction of the suspension wire and M_f is the component of the torque due to eventual mechanical internal friction, inherent in the pendulum system, and not intern to the fluid. There are no terms due to internal stress in the fluid, as well as internal friction in the fluid, because they are not applied on the

rotational pendulum whose static equilibrium is considered. Any elastic reaction relating to elastic deformation of the like-solid phase is considered contained in τ_y (or rather inherent to the contact shear stress itself).

In conclusion, the simple theory of the experiment provides:

$$\tau_y = \frac{(B\,\mu\cos\theta_e - K\theta_e - M_f)}{S_d} \qquad (3)$$

from which the yield stress value can be calculated by measuring the equilibrium angle θ_e, being known all the other parameters on the right side of the equation.

10.2 Temporal trends to spontaneously re-establish conditions of static equilibrium starting from flow condition: measurement of dynamic yield stress

To measure the dynamic yield stress, a first experimental investigation was devoted to the detecting of the rotation angle as a function of time. A torsion was produced up to a maximum fixed angle θ_{max}. Afterwards, the pendulum was left under the sole action of the elastic moment recall and the rotation angle has been acquired while the static equilibrium conditions were restored.

With reference to Figure 19a, initially the pendulum, free from any torsional stress, was stationary at the initial angle θ_i=0. By a slow progressive increase in the intensity of the **B** field along Z axis, the pendulum rotation was produced up to θ_{max}=60°. Then, B was turned off and the rotation of the pendulum, during the approach to the new equilibrium position, was detected over time.

If the experiment is carried out in the air, the pendulum has damped oscillations and gradually stops at the equilibrium angle $|\theta_e| < 0.25°$. This means that the torque due to the internal friction in the pendulum system (M_f) is negligible, since it is included in the limit of the experimental error.

When Carbopol solution is present, after an abrupt decrease of the angle in few seconds, a non-zero equilibrium angle θ_{min} is slowly reached, as shown in Figure 20 for different weight percentage: this clearly indicates that a shear stress occurs on the fluid-cylinder interface, preventing further sliding and balancing the mechanical moment of the elastic recall. Since the fluid initially is flowing and in final condition is stopped, we can speak of dynamic yield stress.

Taking into account that θ_{min} is progressively reached by a counterclockwise rotation and B is switched off, the equilibrium of torques provides:

$$K\theta_{min} - \tau_{yd} \cdot S_d = 0 \qquad (4)$$

$$\tau_{yd} = \frac{K\theta_{min}}{S_d} \qquad (5)$$

where τ_{yd} is the dynamic yield stress.

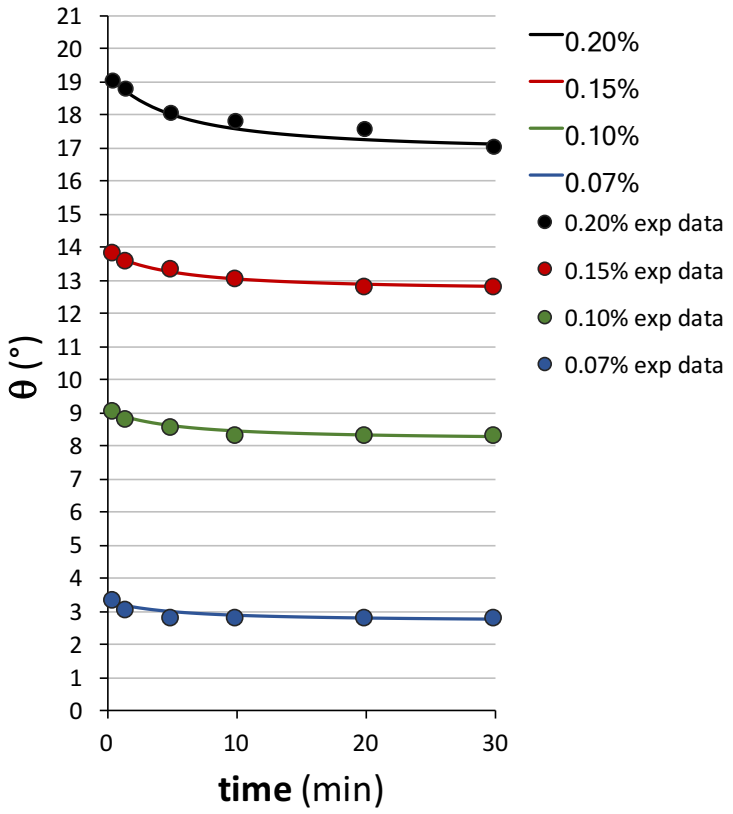

Figure 20: Decrement with time of the rotation angle during the return to the equilibrium condition, under the sole action of the moment of elastic recall. The experimental points are related to different Carbopol contents as specified in the box in the figure and refer to average θ values obtained by repeated measurements. Experimental errors are contained in the point size. Continuous curves are obtained by the analytical simulation described in the text.

In Figure 20 the decreasing behaviors of θ (measured by the MR sensor) with time, starting from θ_{max} in the release position up to θ_{min} in the final equilibrium position, are reported in the aqueous solutions of Carbopol with different weight percentages. The experimental points are obtained by averaging on reiterated measurements and are reported with the respective experimental errors. In general, it appears that after about 20 min the equilibrium is definitively reached in all the used dilutions.

The value of the parameter h was fixed at 3mm for all samples, except for the 0.07%wt solution for which it was necessary to use h=9mm in order to lengthen the evolution times towards the static equilibrium. From the measured values of θ_{min} (Table I), the shear stress values, due to a dynamic yield, have been obtained by applying equation (5).

Table 3*:* Average values of the dynamic yield stress τ_{yd} versus the content of Carbopol as deduced from the final equilibrium angle (θ_{min}) applying equation (5). The errors concerning τ_{yd} were evaluated by means of the propagation law considering the sensitivity of the measuring devices.

Weight percentage of Carbopol (%)	**0.07**	**0.10**	**0.15**	**0.20**
θ_{min} (°)	**2.75±0.25**	**8.25±0.25**	**12.75±0.25**	**17.00±0.25**
τ_{yd} (10^{-1} Pa)	**1.8 ± 0.3**	**11.8 ± 0.7**	**18.2± 0.7**	**24.3 ± 0.7**

When stopping from flow to static condition, Carbopol solutions change both the microscopic morphology and the physical properties from liquid-like to solid-like [1, 39]. The establishment of a new structural configuration with different physical and chemical properties could take time, and this phenomenon is relevant in enhancing thixotropic behavior [2]. Therefore, in studying the settling down of the equilibrium starting from a kinetic condition, in order to identify the dynamic yield stress, the approach to equilibrium takes time, as evidenced by the experimental results in Figure 20. Considering the used measurement methodology, it is important to note that, when the cylinder IC (Figure 18) is approaching to stop, the fluid in contact with the surface of the cylinder acquires a zero velocity relative to the cylinder itself. The fluid in the cavity of the two cylinders follows the classical shear flow profile, where the velocity is zero at the fixed wall and is

maximum at the moving wall. So, the fluid velocity takes some time to become zero everywhere. Only when the shear-flow completely ends, the cylinder IC is blocked.

It is interesting to stress from Figure 20 that practically the same time occurs to reach equilibrium in solutions at different Carbopol contents (for all dilution, 20 minutes are necessary to make the decrement of θ lower than the experimental error). This indicates that the processes governing the time evolution are the same in all the cases. Since by increasing Carbopol content both viscosity, η, and elastic modulus, G', increases it is plausible that the relaxation time of the equilibrium approach results practically the same, being related to the ratio η/ G', as generally results in polymers. On the other hand, the absolute decrement appears to be linked to a different composition and consequent different viscosity and density, since they are not proportional to the content only [78, 96, 97].

10.3 Effect of the application of an external torque to start a flow from the initial equilibrium condition at θ=0: determination of the static yield stress

In the absence of liquid, starting from θ = 0, the current in the Helmholtz coils is increased to produce a magnetic induction field that applies a mechanical moment $\boldsymbol{\mu} \wedge \mathbf{B}$ to the torsional pendulum (**B** is applied along Z; see Figure 19). Since the rotation starts at the lowest applicable current, the mechanical moment, due to the internal friction of the pendulum, is negligible to inhibit rotation, in agreement with what was observed about the free oscillations in the previous Section 3.1.

Then, starting from the pendulum in the initial equilibrium position (θ= 0 and B=0) and with the fluid material covering the rotating cylinder up to a height h, a magnetic induction field $B = N \cdot \Delta B$ is applied, with $\Delta B = 0.25 \cdot 10^{-5}$ T and N increased progressively by one unit. After 20 minutes from B application, the rotation angle detected by the sensor MR (Figure 19a) was recorded, verifying that after this wait the stable equilibrium is obtained (the measured values of θ_e *vs* B remain stable over time). In presence of a static yield stress the pendulum rotation is counteracted and the pendulum remains at rest up to $B \leq B^0$. In other words, only for $B = B^0 + \Delta B$ a permanent rotation, equal to or greater than the minimum detectable one ($\Delta\theta = 0.25°$ by means of MR sensor), is detected. We have outlined "permanent" rotation, because it was always verified that by decreasing magnetizing induction field, namely returning towards B=0T value, the rotation does not return to zero. In fact, if the equilibrium angle equal zero is restored, it means that the investigated solution is strained (as in an elastic solid sample) but no flow is produced. Only if rotation does not return to zero by removing magnetic induction field we consider activated the flowing fluid adjacent to the rotating cylinder surface.

This is clarified by the data represented in Figure 21. In fact, if a torsional cycle is performed up to B° to successively return to zero, also the rotation angle goes to zero; on the contrary, when the maximum B value is shifted to $B° + \Delta B$ the rotation remains partially permanent when the torsion returns to zero (Figure 21).

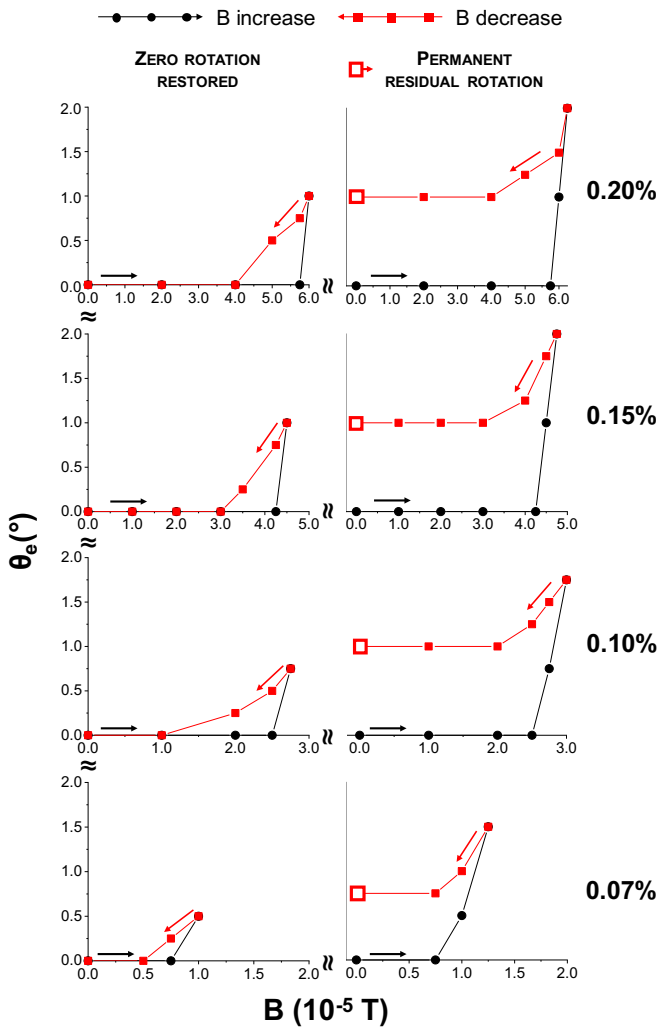

Figure 21: For each solution with different Carbopol content both the torque cycles, θ_e vs B, up to a maximum value B^o and return to zero (on the left) and the torque cycle up to a maximum $B^o + \Delta B$ and return to zero (on the right) are shown: in the first case the rotation is completely reverted, in the second a residual rotation is found. This indicates that B^o applies a torque producing a solid-like material deformation, which can be reverted decreasing B to zero, instead a minimum B^o increment (ΔB) produces an greater torque which induces a flow activation with a liquid-like response, and consequently an effective rotation of the cylinder inside the fluid. In fact, the rotation is not eliminated by reducing the torsional stress to zero.

Once one finds the B^o value, by applying the equilibrium conditions (3) to the sum of the mechanical moments, with $M_f = 0$, we can deduce the static yield stress:

$$\tau_{ys} = \frac{B^\circ \mu \cos\theta_e - K\theta_e}{S_d} \qquad (7)$$

taking into account the S_d value for h=3 mm, except in the case of 0.07% wt solution for which h=9mm was used. This last choice was necessary otherwise the pendulum rotation starts for values of the magnetic induction field very close to the minimum instrumentation limit making it impossible to identify the threshold value B°.

In Table II the values of B° are reported with the consequent τ_{ys} values obtained from equation (7). The percentage difference between static and dynamic yield stress ($\Delta\tau/\tau_{yd}$) is also shown. The static conditions give higher values for all Carbopol content supporting the conclusion that the difference depends on the procedure only and it is not an intrinsic property of the material.

Table 3: For each aqueous Carbopol solution, the table shows the B° field value deducted from the torque cycles ($\square_e$ vs B) in figure 4, the static yield stress consequent from equation (7) and the percentage increase ($\square\square\square\square_{yd}$) of the static value with respect to the dynamic one. The errors concerning $\square_{ys}$ were evaluated by means of the propagation law considering the sensitivity of the measuring devices.

Carbopol weight percentage	**B° (10^{-5}T) ± $0.25\cdot10^{-5}$ T**	**τ_{ys} (10^{-1} Pa)**	**$\Delta\tau/\tau_{yd}$ (%)**
0.07 %	**1.00**	**1.9 ± 0.6**	**6%**
0.10 %	**2.75**	**12.3 ±1.4**	**4%**
0.15 %	**4.50**	**20.5 ±1.4**	**13%**
0.20 %	**6.00**	**27.8 ±1.4**	**14%**

In fact, the lower value of dynamic yield stress can be understood by considering that the kinetic rotational energy of the pendular system must be canceled by the work of the fluid shear reaction forces and this work is made by the elastic reaction of the like-solid material that is forming, so straining it and abating the equilibrium angle, θ_{min}. As consequence, an artefact decrement of yield stress measured from equation (5) is produced. This effect is inactive in the static case, when only structure yielding is present. This means that there are not two different yield stresses, but that the stress value depends strictly on the measurement initial conditions: dynamic or static. This work is published on Rheologica Acta [98] .

11 Experimental investigation on foam formation through deformable porous media

During the PhD, working in collaborations with Brussels Innovation center of P&G, we studied the foam formation in deformable porous media as kitchen sponges.

11.1 Background

Foams are complex materials structured at different length scales, from micro- to macro-scale [99-101]. Thanks to their peculiar structure, foams have gained attention in different fields of applications, from everyday life care (i.e. food/cosmetic/detergent) to oil recovery and automotive industries [102-105]. A foam is made of gas bubbles dispersed in a continuous aqueous phase stabilized by surface active molecules adsorbed at the gas/liquid interface [106, 107]. There are many ways to form foams, by gas entrainment or bubbling into the liquid [108], or by the injection of gas and aqueous solution of surfactants into a porous medium [109, 110], the latter strongly affecting foam properties, in terms of microstructure and material.

In the last decades, foam generation and flow in confined systems [111], such as porous media [112], have drawn much interest due to the industrial implications, especially in enhanced oil recovery (EOR). Indeed, since the 1960's [113] many experimental studies have showed that foams play a key role in EOR, drastically reducing gas mobility in porous media from about 50% to less than 1% [114, 115]. This is strictly related to foam

texture [116] and it is basically due to the fact that foam traps a large fraction of the gas in place, then increasing the resistance of gas present among rocks to flow. Foam formation and flow in porous media has been also investigated numerically, starting from the pioneering study of Falls [117] in the 1980's, and several models have been developed in the last three decades based on mechanistic, semi-empirical and empirical approaches [118, 119].

An additional complexity can be given when pores are deformable, like in sponges, where pore size, connectivity and shape change with the application of an external stress. To model the mechanism behind bubble break up during foaming, the Weber dimensionless number (We) has been used extensively [120-122]. In fact, We number correlates the inertial force causing bubble deformation and the surface tension force acting to restore bubble sphericity. For example, bubble breakup occurs when the external forces on bubbles make We>1. However, this number, though quite meaningful to describe the behavior of foam formation in porous media, is not equally useful in the case of deformable porous medium because it doesn't take into account the effect of pores deformation, the surfactant rearrangement on bubble surface during foam formation, and the energy required to create a gas/liquid interface, which has a critical effect on foam stability [123]. Due to the complexity of the matter, the coupled problem of the flow of a complex system, such as a foam, in a deformable porous media, has only been studied

from a modeling point of view [124, 125] whereas to our knowledge experimental investigations are still lacking.

This work was addressed to the investigation of foam formation *in situ* in a deformable porous medium, like the typical sponges used in dishwashing, placing the emphasis on the effect of surfactant concentration and sponge material in foaming performance. In particular, foam formation into a synthetic sponge is firstly investigated with a focus on the effect of confinement on mean bubble diameters, and the results are compared with data obtained in unconfined conditions. Furthermore, a comparison between the foam formed through a synthetic sponge and foam obtained from a cellulose sponge was carried out by highlighting the influence of porous media microstructure and material on foam properties. The experimental results presented in this work provided valuable and critical insights about foam formation in deformable porous media, which is still an open issue of strong interest in several industrial applications. These results have been published in the Canadian Journal of Chemical Engineering [126].

11.2 Materials and Methods

Materials

The solutions used in this work are made of surfactant (sodium laureth sulphate – SLE_3S) and water at different concentrations (1, 5, 10% w/w). SLE_3S is an anionic surfactant

found in many personal care products and detergents for their cleaning and emulsifying properties, being a very effective foaming agent. SLE_3S chemical formula is CH3(CH2)11(OCH2CH2)3OSO3Na and its critical micellar concentration (CMC) is about 0.2 [g/ L^{-1}], so that all the surfactant concentrations investigated in this work are far above the CMC. The equilibrium surface tension in such range of concentrations is a constant value equal to ~ 27 [mN/m].

A stock solution of 70% wt/wt of SLE_3S has been provided by Procter and Gamble, and aqueous solutions have been prepared by dissolving the detergent in water at different concentrations, by mixing in a beaker on a magnetic stirrer at low energy and room temperature.

Commercial synthetic and cellulose sponges (from Scotch-Brite) are used as porous media. The typical synthetic sponge used in detergency is made of a polyurethane solid foam, while the cellulose one is made of vegetable fibers.

Experimental setup

Dry synthetic sponge structure is visualized by stereomicroscopy (Axiovert 200 M - Zeiss) and by optical microscopy (Zeiss Axiovert 100) by using low magnification objectives (EC Plan-Neofluar 1.25x/0,08, LD Epiplan 10x/0,25 DIC and LD A-Plan 20x/0,03 Ph1). Then, in order to visualize foam formation through the sponge, two experimental setups, one confined and the other unconfined, have been built (Figure 1). The former is made of

two parallel glass coverslides, while the latter is made of a glass coverslide on the bottom side and a net, with a given mesh, on the upper side. A sponge of fixed volume (2.0 × 1.5 × 0.5 cm) is placed between the two coverslides (or coverslide and net). A schematic representation of the experimental set-up is shown in Figure 22.

The experiments are performed by soaking the sponge in a premixed surfactant solution at a certain concentration. Then, the sponge is squeezed several times in the confined/unconfined system, fixing the squeezing time at 1s and sponge compression at 80%, the latter being the maximum possible compression of the sponge. Once enough foam to be analyzed is formed, mean bubble size at the sponge interface is analysed.

Images of bubble formation are acquired by using a confocal laser scanning microscope (LSM 5 Pascal, Zeiss), a stereomicroscope, and an inverted optical microscope equipped with a high-speed camera (Phantom 4.3) allowing to acquire up to 1000 frame/seconds in the field of view investigated. The extracted images are analyzed by a software of image analysis (Image Pro-plus) and measurements of bubble mean diameter of the foam are performed at each squeeze, by selecting an image area close to the sponge interface. For each squeeze, at least 100 bubbles are analysed.

The investigation of foam fractal dimension are carried out by using a Matlab algorithm based on a box-counting method (more details can be found in “Preziosi et al., Flow-induced nanostructuring of gelled emulsions, Soft Matter, 2017, 13, 5696-5703”[127]).

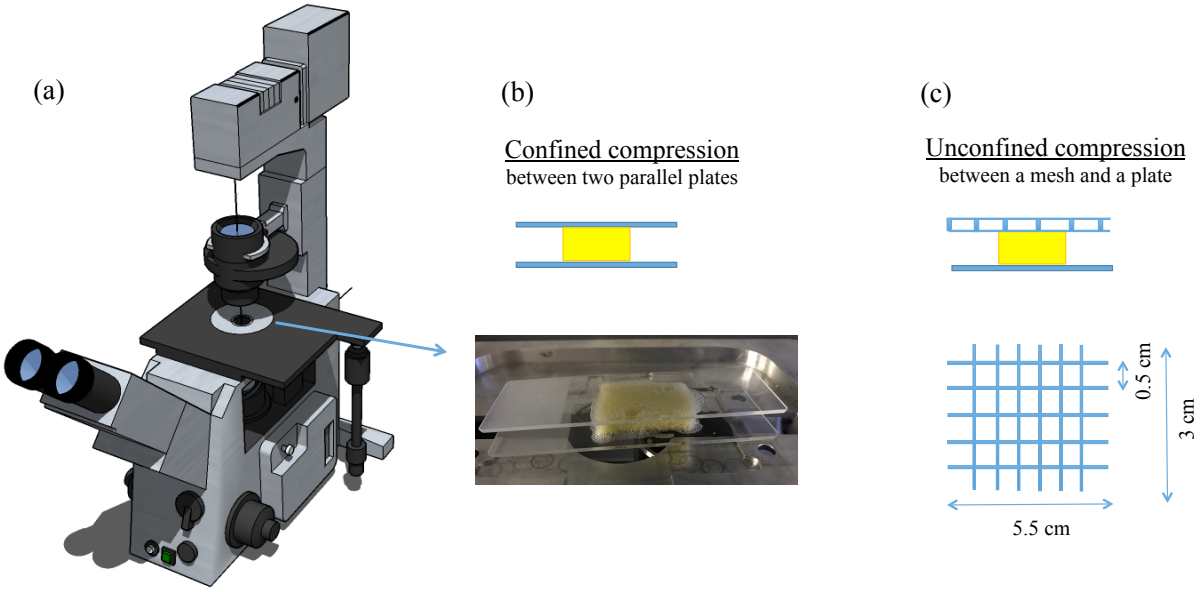

Figure 22: Experimental setup. (a) Schematic of the microscope. Compression systems. (b) Confined compression between two coverslides and (c) Unconfined compression between a mesh and a coverslide

Synthetic sponge

A characterization of the structure of the synthetic sponge has been performed by stereomicroscopy (Figure 2), finding different microstructures for the yellow and green side of the sponge. In particular, the yellow side, made of a polymeric foam, shows a regular structure (Figure 23a), while the green side is made of an interconnected and filamentous net with an irregular fiber network (Figure 23b). A deeper insight into the sponge yellow side microstructure performed by optical microscopy at different magnifications shows the presence of pores with size in the order of hundreds of microns (~ 400 μm) and confirms a quite regular geometry (Figure 23d). Pore size distribution of the dry synthetic sponge (yellow side) is reported in the histogram of Figure 23e.

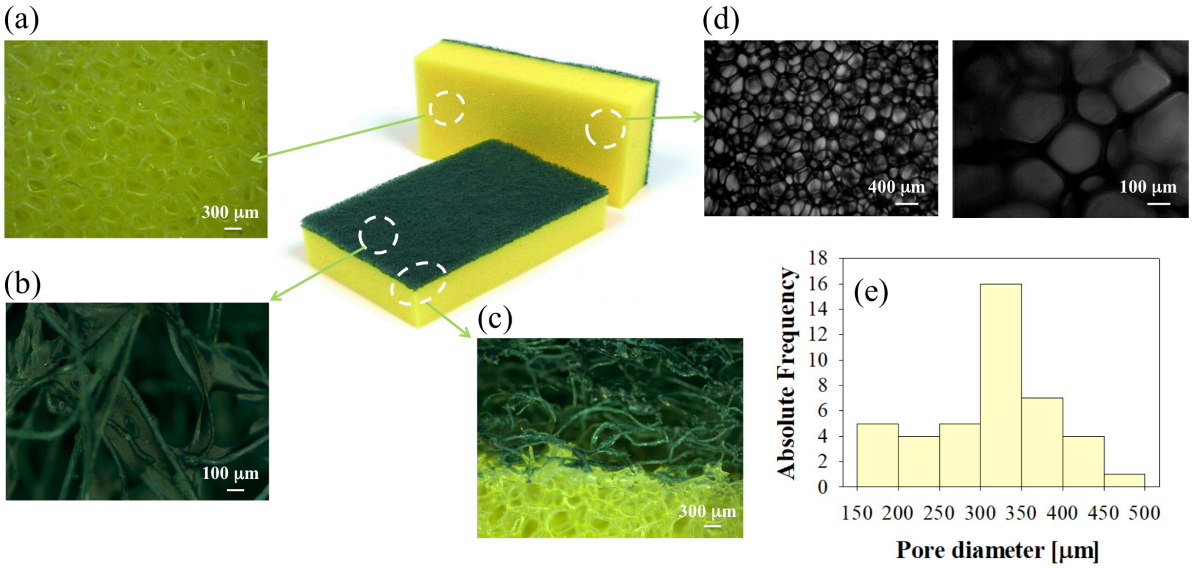

Figure 23: Microscopy characterization of the dry synthetic sponge. (a-c) By stereomicroscopy and (d) by optical microscopy. (d) Histogram reporting pore size distribution of sponge yellow side

Experimental investigation of foam formation through a synthetic sponge has been performed at three detergent concentrations, 1, 5 and 10% w/w. Such premixed solutions are added onto the sponge which is put between the two cover slides (confined configuration). After that, the sponge is squeezed several times (i.e., 3, 7 and 9 times). The panel in Figure 24 illustrates foam formation for the three solutions and at different squeezes (3rd, 7th and 9th squeeze), showing bigger bubbles formed at the surface of the sponge after few squeezes, while, as the number of squeezes increases, bubbles break when the solution is sucked back in the pore network leading to smaller bubbles at the exit from the sponge).

A bubble size gradient from the sponge surface can be observed and it can be attributed to the larger size of the initially formed bubbles. As the number of squeezes increases, bubbles tend to break and become smaller (see Figure 24). In addition, the panel shows how detergent concentration affects mean bubble diameter; in fact, higher detergent concentration leads to the formation of foam with smaller bubbles even at low number of squeezing. In all cases, the foams so obtained can be classified as wet foams, which are made of a high volume fraction of liquid; indeed, liquid volume fraction ϕ_L of the system at 1%w/w detergent concentration, at high number of squeezes, has been estimated by image analysis as equal to ~ 0.6.

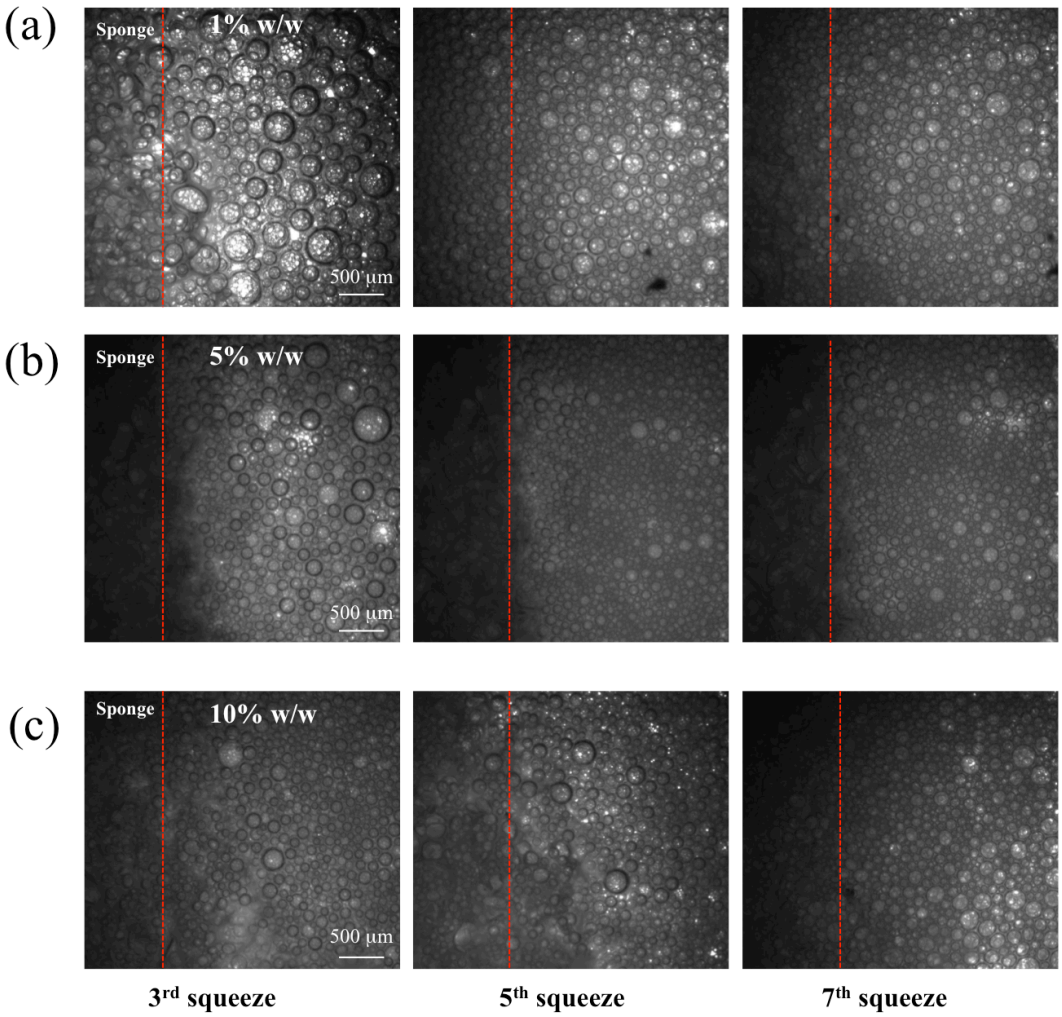

Figure 24: Investigation of foam formation in the confined system at 1, 5 and 10% w/w detergent concentration as a function of the number of squeezes

Analysis of foam bubbles size is reported in Figure 25 in particular, histograms with bubble size distribution as a function of number of squeezes for the system at 1% w/w detergent is shown in Figure 24a, confirming the trend of the images reported previously (Figure 23a). A mean bubble diameter decrease upon sponge compression is observed in the plot for the three concentrations investigated (Figure 25b). Indeed, the three curves show that the initial foam is made of larger bubbles whose size decreases as sponge

compression increases. Although the surface tension is a constant value, as surfactant concentration increases the value of bubble mean diameter decreases. At high numbers of squeezing, bubble size is in the order of hundreds of microns reaching an apparent plateau value, as shown by the curves in Figure 25b.

The analysis of foam fractal dimension, D_f, at the three investigated concentrations is also reported (Figure 24c). The fractal dimension can be defined as a measure of the degree of irregularity of a system. In particular, in foams it can be related to the distribution of gas in the liquid[128]. In our case, confocal images have been converted in black and white ones by using image analysis software and by using a Matlab algorithm, D_f has been measured at each squeeze and at 1, 5 and 10% surfactant concentration. It has been observed that the gas distribution in the foam does not change during the squeezing process, thus suggesting that the bubble size variation is just connected to the mechanical deformation induced by the sponge porosity and deformation and not by a change in gas volume fraction. In fact, as observed in the plot in Figure 24c, the fractal dimension stays almost constant around the value of 1.7, as a function of the number of squeezings.

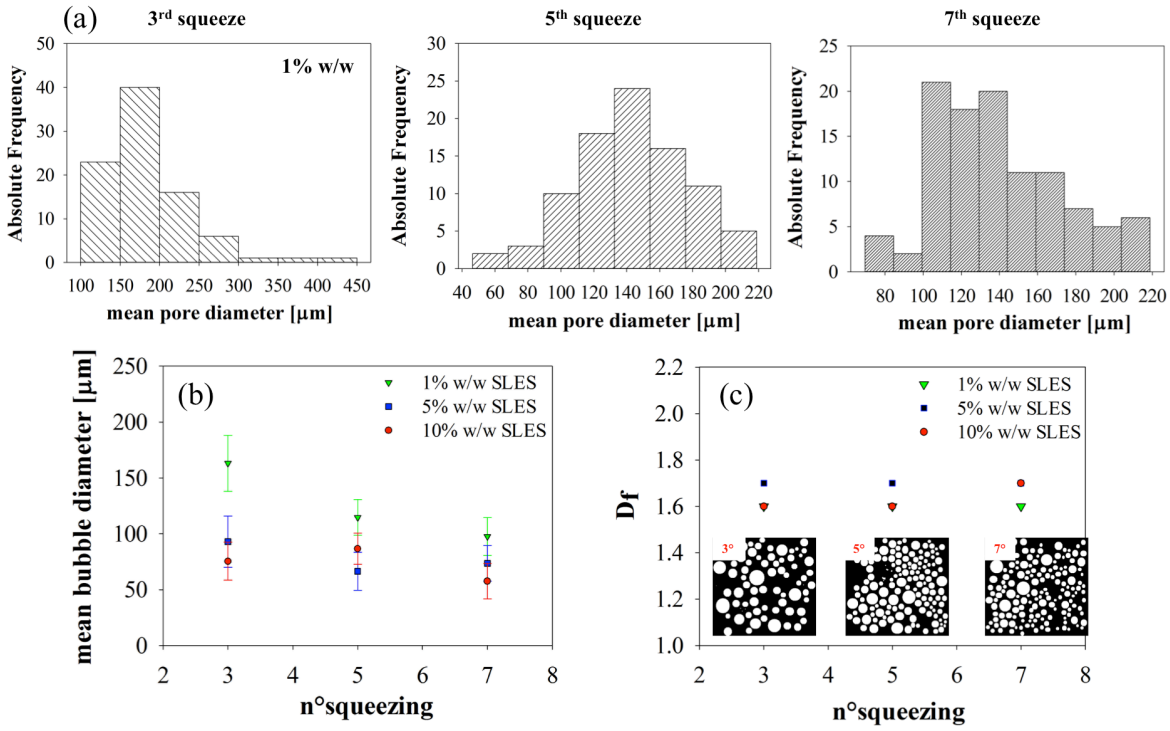

Figure 25: (a) Bubble size distribution for the system at 1% w/w detergent at three squeezes. Histograms are numerical distributions of bubble diameters. (b) Plot reporting mean bubble diameter as a function of number of squeezes for the three concentrations investigated. (c) Plot reporting fractal dimension D_f as a function of number of squeezes

To reduce the effect of confinement, the investigation of foam properties under compression of a net has been carried out. The evolution of foam formation in the unconfined configuration is shown in Figure 25a for the system at 1% w/w detergent, which exhibits bigger bubbles (~200 μm at foam formation) with the respect to the ones formed in the confined system (~100 μm), the difference being probably to be imputed to the different amount of sucked air and to the less uniform compression occurring in the open system. Indeed, experimental results show that in such open configuration the sponge needs to be squeezed more times with respect to the confined system before

enough foam is formed. In Figure 25 the foam formed in the open configuration has been analyzed in terms of liquid volume fraction and a lower value of ϕ_L with the respect to the one obtained in the confined system, has been found ($\phi_L \sim 0.45$). It is worthwhile to observe that the foam produced in daily-life situations such as during dishwashing operations, is typically a quite dry foam characterized by a low fraction of liquid ($\phi_L < 0.3$), which is more similar to the foam produced in the open configuration than the one produced in the confined system.

A quantitative analysis of mean bubble size as a function of number of squeezes in the open system is also reported in Figure 25b, showing a slightly decreasing trend until a plateau value ($\sim 200\ \mu$m) is reached.

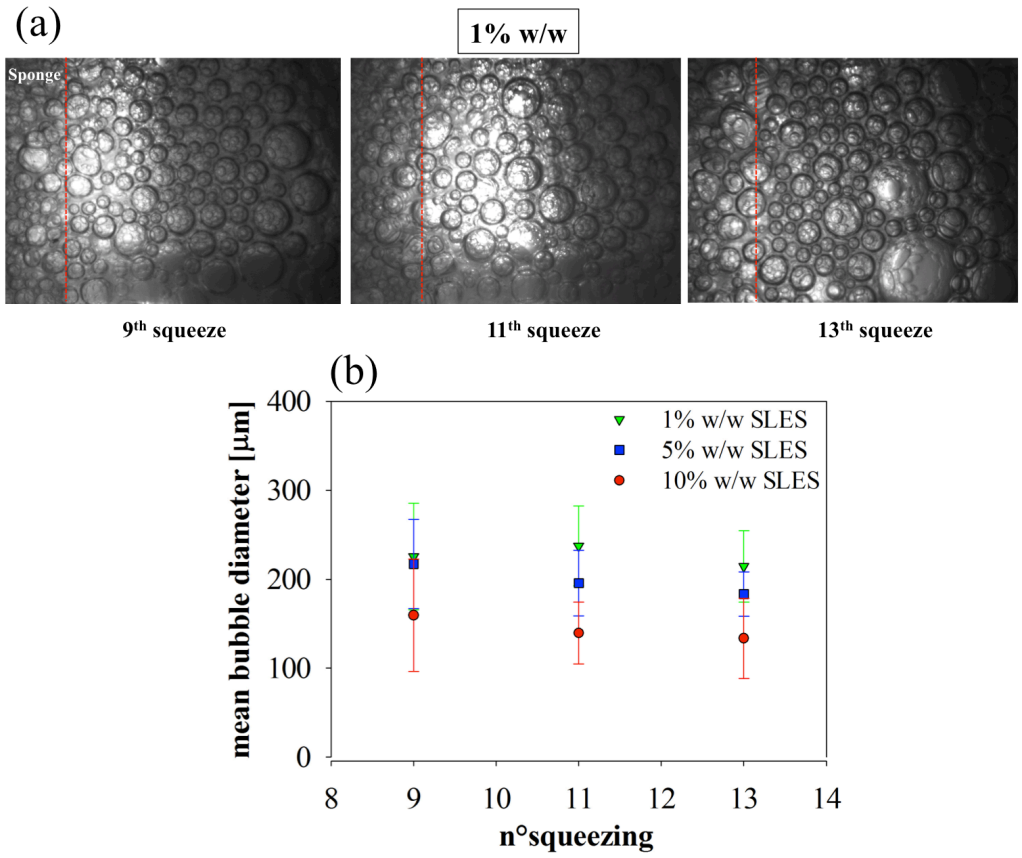

Figure 26: (a) Sequence of images showing foam formation in the unconfined system at the three concentrations investigated, 1, 5 and 10% w/w; (b) Plot reporting mean bubble diameter vs n° squeezes

Cellulose sponge

To investigate the effect of sponge material on foam formation, a common cellulose sponge has been observed under the optical microscope. A quite different microstructure with respect to the synthetic sponge is found. The microstructure is characterized by a dense filamentous configuration interconnected with wide empty areas, as shown in Figure 26 (a-b), where a comparison with the synthetic in terms of microstructure is reported.

Further comparisons between the two sponges have been carried out; in particular, observations of water absorption are reported in Figure 26 (c-d). Water is added dropwise to the sponges and the images, acquired with a high definition camera (Canon Eos D60), show that in the case of the cellulose sponge, the droplet immediately penetrate through it (even swelling the sponge), while in the case of the synthetic sponge, the droplet stays on the surface suggesting a much more hydrophobic character. So, for the latter case the contact angle between a water droplet and the sponge surface has been measured, and a value of ~ 82° was found, thus confirming that the synthetic sponge is much more hydrophobic than the cellulose one. Indeed, one of the main differences between the two sponges is the amount of surfactant solution used to form the final foam; in fact, the cellulose sponge has the capability to trap part of the water solution, so in order to produce the same amount of foam as with the synthetic sponge, we had to increase the amount of added liquid.

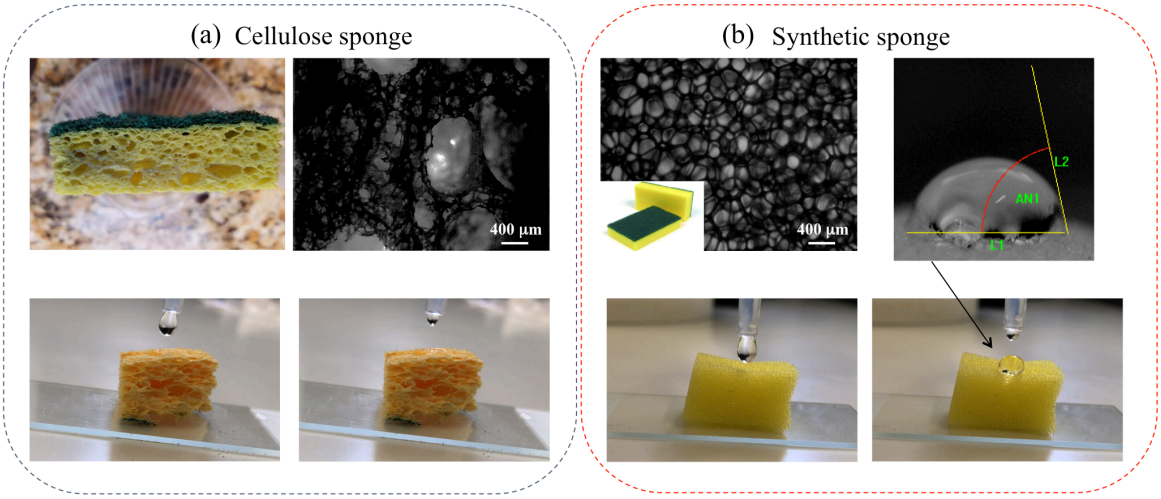

Figure 27: Comparison between the (a) cellulose and (b) synthetic sponge. Optical microscopy showing sponge microstructures and contact angle experiments are reported

Experiments on foam formation dynamics confirms that bubble size in the case of the cellulose sponge is different from the ones obtained with the synthetic sponge. In particular, bubbles are much smaller than before, as clearly observed in Figure 27a, most likely due to the different sponge microstructure. A panel reporting foam formation during squeezing of the solution at 1% w/w detergent by using the cellulose sponge shows the presence of a bubble size gradient away from the sponge surface and the formation of bubbles with a mean size in the order of 60 μm at high number of squeezing. The comparison between foam bubble sizes at the (cellulose/synthetic) sponge surface is highlighted in Figure 27b, where a strong difference between the two cases is shown. In particular, even though the trend is similar, bubbles of the foam formed in the cellulose sponge are much smaller than the bubbles formed in the synthetic one.

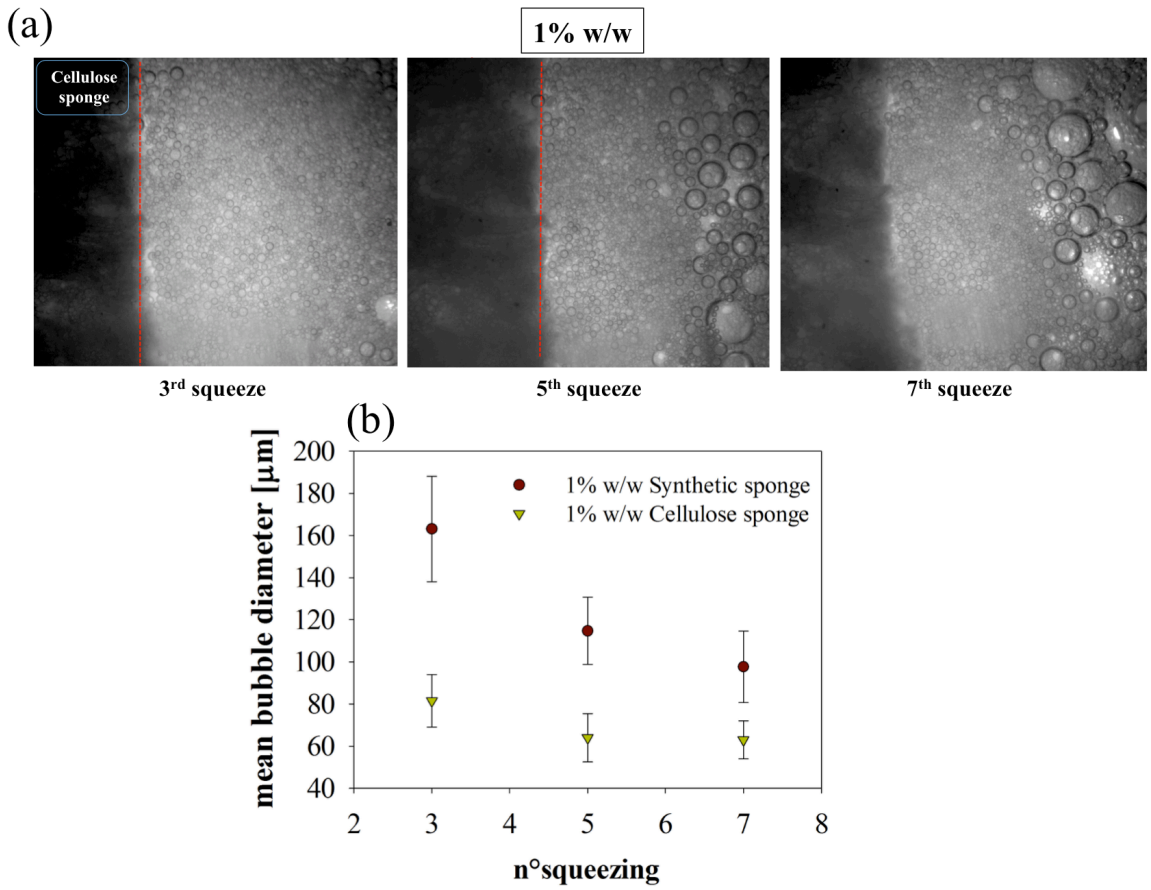

Figure 28: Foam formation in the confined system. Comparison between the synthetic and cellulose sponge at 1% w/w detergent. (a)Panel reporting optical imaging at three squeezes, (b) Plot reporting mean bubble diameter *vs* n° squeezes

12 Conclusions

This study was addressed to investigate complex fluid such as polyacrylic acid in water, or foams and their interactions with porous media.

Confocal imaging allowed to look at system microstructure in static conditions and at different concentrations, providing evidence of micrometric particles and their dendritic-like aggregates at increasing Carbopol concentrations.

Lately, microscopy was used to investigate the phase behavior of the system at different temperature, building an initial phase diagram in which is possible to observe the miscibility gap. The system seemed to behave as a UCST, a trend that can be observed in other polymer systems in particular associative polymers.

Microscale investigations were also compared with classical flow characterization to understand the effect of flow and confinement (glass tube of micron size as model porous media) on the microstructure. Hence, it was possible to highlight a remarkable redistribution of the Carbopol particles along the geometry, effect that can explain the strong differences between classical rheological measure of the yield stress and capillary flow estimation.

NMR-MOUSE proof of concept for studying Non-Newtonian liquid flow in porous media it has been realized, showing that quantitative test can be performed. This technique will allow in the future to experimentally validate modeling of real porous media flow of complex liquids.

A novel technique for measuring yield stress in Carbopol gels was also developed and used in collaboration with the department of Physics of the University Federico II. The system allowed to identify doing just one single test both static and dynamic yield stress.

The proposed MFATPT technique fits in the field of rotational shear rheometry in concentric cylinders geometry. Compared to standard methodologies, its main points of innovation are the alternative direct physical approach, the effectiveness of the magnetic field assistance, the possibility of adjusting the measurement to the specific time

dependency in the YSF used and the ability to measure dynamic and static yield stress with the same experimental setup. These prerogatives strongly candidate the new methodology to highlight and elaborate peculiar aspects in yield stress fluids.

In the end an alternative system, as a model detergent, was studied to investigate foam formation in deformable porous media as kitchen sponges. A microscopical investigation allowed to visualize the foam formation and the effect of surfactant and sponge material on the foam generated. Our results showed that the foam obtained is made of very heterogeneous bubbles, in particular, after sponge squeezing, large bubbles are formed at the surface of the sponge and a bubble size gradient is observed away from sponge surface. With respect to the confined system, the open configuration led to the formation of foams having bigger bubbles, more similar to some cases occurring in daily life, i.e. dishwashing. Furthermore, the effect of sponge material was investigated, and differences in the foaming performance were found, likely due to different hydrophobicity and microstructure.

13 Bibliography

[1] D. Bonn, M.M. Denn, L. Berthier, T. Divoux, S. Manneville, Yield stress materials in soft condensed matter, Reviews of Modern Physics 89(3) (2017) 035005.

[2] M. Dinkgreve, M. Fazilati, M. Denn, D. Bonn, Carbopol: From a simple to a thixotropic yield stress fluid, Journal of Rheology 62(3) (2018) 773-780.

[3] M. Agarwal, Y.M. Joshi, Signatures of physical aging and thixotropy in aqueous dispersion of Carbopol, Physics of Fluids 31(6) (2019) 063107.

[4] A.Z. Nelson, R.E. Bras, J. Liu, R.H. Ewoldt, Extending yield-stress fluid paradigms, Journal of Rheology 62(1) (2018) 357-369.

[5] N.J. Balmforth, I.A. Frigaard, G. Ovarlez, Yielding to stress: recent developments in viscoplastic fluid mechanics, Annual Review of Fluid Mechanics 46 (2014) 121-146.

[6] P. Coussot, Rheometry of pastes, suspensions, and granular materials: applications in industry and environment, John Wiley & Sons2005.

[7] P. Coussot, Bingham's heritage, Rheologica Acta 56(3) (2017) 163-176.

[8] P. Coussot, L. Tocquer, C. Lanos, G. Ovarlez, Macroscopic vs. local rheology of yield stress fluids, Journal of Non-Newtonian Fluid Mechanics 158(1-3) (2009) 85-90.

[9] A.M. Putz, T.I. Burghelea, The solid–fluid transition in a yield stress shear thinning physical gel, Rheologica Acta 48(6) (2009) 673-689.

[10] D. Doraiswamy, A. Mujumdar, I. Tsao, A. Beris, S. Danforth, A. Metzner, The Cox–Merz rule extended: a rheological model for concentrated suspensions and other materials with a yield stress, Journal of rheology 35(4) (1991) 647-685.

[11] D. Lee, I.A. Gutowski, A.E. Bailey, L. Rubatat, J.R. de Bruyn, B.J. Frisken, Investigating the microstructure of a yield-stress fluid by light scattering, Physical Review E 83(3) (2011) 031401.

[12] J. Pérez-González, J.J. López-Durán, B.M. Marín-Santibáñez, F. Rodríguez-González, Rheo-PIV of a yield-stress fluid in a capillary with slip at the wall, Rheologica acta 51(11-12) (2012) 937-946.

[13] R.P. Chhabra, Non-Newtonian fluids: an introduction, Rheology of complex fluids, Springer2010, pp. 3-34.

[14] J.M. Krishnan, A.P. Deshpande, P.S. Kumar, Rheology of complex fluids, Springer2010.

[15] C.W. Macosko, Rheology Principles, Measurements and Applications (1994).

[16] R.P. Chhabra, J.F. Richardson, Non-Newtonian flow and applied rheology: engineering applications, Butterworth-Heinemann2011.

[17] E.C. Bingham, An investigation of the laws of plastic flow, US Government Printing Office1917.

[18] W. Ostwald, R. Auerbach, Ueber die Viskosität kolloider Lösungen im Struktur-, Laminar-und Turbulenzgebiet, Kolloid-Zeitschrift 38(3) (1926) 261-280.

[19] T.G. Mezger, The rheology handbook: for users of rotational and oscillatory rheometers, Vincentz Network GmbH & Co KG2006.

[20] M. Doi, Introduction to polymer physics, Oxford university press1996.

[21] P.-G. De Gennes, P.-G. Gennes, Scaling concepts in polymer physics, Cornell university press1979.

[22] G.C. Berry, T.G. Fox, The viscosity of polymers and their concentrated solutions, Fortschritte der Hochpolymeren-Forschung, Springer1968, pp. 261-357.

[23] R.B. Bird, R.C. Armstrong, O. Hassager, Dynamics of polymeric liquids. Vol. 1: Fluid mechanics, (1987).

[24] P.J. Carreau, Rheological equations from molecular network theories, Transactions of the Society of Rheology 16(1) (1972) 99-127.

[25] S. Curran, R. Hayes, A. Afacan, M. Williams, P. Tanguy, Properties of Carbopol Solutions as Models for Yield-Stress Fluids, Journal of food science 67(1) (2002) 176-180.

[26] N. Alderman, G. Meeten, J. Sherwood, Vane rheometry of bentonite gels, Journal of non-newtonian fluid mechanics 39(3) (1991) 291-310.

[27] P. Coussot, Q.D. Nguyen, H. Huynh, D. Bonn, Avalanche behavior in yield stress fluids, Physical review letters 88(17) (2002) 175501.

[28] H. Barnes, K. Walters, The yield stress myth?, Rheologica acta 24(4) (1985) 323-326.

[29] W.H. Herschel, R. Bulkley, Konsistenzmessungen von gummi-benzollösungen, Colloid & Polymer Science 39(4) (1926) 291-300.

[30] J. Piau, Carbopol gels: Elastoviscoplastic and slippery glasses made of individual swollen sponges: Meso-and macroscopic properties, constitutive equations and scaling laws, Journal of non-newtonian fluid mechanics 144(1) (2007) 1-29.

[31] M.A. Rao, J.L. da Silva, Role of rheological behavior in sensory assessment of foods and swallowing, Rheology of Fluid and Semisolid Foods, Springer2007, pp. 403-426.

[32] Y. Li, Z. Zhou, X. Zhao, H. Zhao, X. Qu, The Rheological and Skin Sensory Properties of Cosmetic Emulsions: Influence of Thickening Agents, Journal of cosmetic science 69(1) (2018) 67-75.

[33] Q. Nguyen, D. Boger, Measuring the flow properties of yield stress fluids, Annual Review of Fluid Mechanics 24(1) (1992) 47-88.

[34] J. Chong, E. Christiansen, A. Baer, Rheology of concentrated suspensions, Journal of applied polymer science 15(8) (1971) 2007-2021.

[35] P. Coussot, Yield stress fluid flows: A review of experimental data, Journal of Non-Newtonian Fluid Mechanics 211 (2014) 31-49.

[36] M. Dinkgreve, J. Paredes, M.M. Denn, D. Bonn, On different ways of measuring "the" yield stress, Journal of non-Newtonian fluid mechanics 238 (2016) 233-241.

[37] F. Rouyer, S. Cohen-Addad, R. Höhler, Is the yield stress of aqueous foam a well-defined quantity?, Colloids and Surfaces A: Physicochemical and Engineering Aspects 263(1-3) (2005) 111-116.

[38] D. Bonn, M.M. Denn, Yield stress fluids slowly yield to analysis, Science 324(5933) (2009) 1401-1402.

[39] M. Shafiei, M. Balhoff, N.W. Hayman, Chemical and microstructural controls on viscoplasticity in Carbopol hydrogel, Polymer 139 (2018) 44-51.

[40] W.P. Schellart, V. Strak, A review of analogue modelling of geodynamic processes: Approaches, scaling, materials and quantification, with an application to subduction experiments, Journal of Geodynamics 100 (2016) 7-32.

[41] J.E. Reber, L.L. Lavier, N.W. Hayman, Experimental demonstration of a semi-brittle origin for crustal strain transients, Nature Geoscience 8(9) (2015) 712-715.

[42] S.R. Kwon, P.W. Wertz, Review of the mechanism of tooth whitening, Journal of Esthetic and Restorative Dentistry 27(5) (2015) 240-257.

[43] S. Jain, D.P. Kale, R. Swami, S.S. Katiyar, Codelivery of benzoyl peroxide & adapalene using modified liposomal gel for improved acne therapy, Nanomedicine 13(12) (2018) 1481-1493.

[44] F. Zhang, J. Lubach, W. Na, S. Momin, Interpolymer complexation between Polyox and Carbopol, and its effect on drug release from matrix tablets, Journal of pharmaceutical sciences 105(8) (2016) 2386-2396.

[45] T.U. Wani, N.A. Khan, Formulation of Carbopol Capsules for Sustained Release of Losartan Potassium, Journal of Drug Delivery and Therapeutics 9(2-s) (2019) 92-97.

[46] H.-R. Lin, K. Sung, Carbopol/pluronic phase change solutions for ophthalmic drug delivery, Journal of controlled release 69(3) (2000) 379-388.

[47] S. Ishii, J. Kaneko, Y. Nagasaki, Dual stimuli-responsive redox-active injectable gel by polyion complex based flower micelles for biomedical applications, Macromolecules 48(9) (2015) 3088-3094.

[48] M. Jaiswal, A. Kumar, S. Sharma, Nanoemulsions loaded Carbopol® 934 based gel for intranasal delivery of neuroprotective Centella asiatica extract: in–vitro and ex–vivo permeation study, Journal of Pharmaceutical Investigation 46(1) (2016) 79-89.

[49] G.P. Roberts, H.A. Barnes, New measurements of the flow-curves for Carbopol dispersions without slip artefacts, Rheologica Acta 40(5) (2001) 499-503.

[50] N. Taylor, E. Bagley, Tailoring closely packed gel–particle systems for use as thickening agents, Journal of Applied Polymer Science 21(1) (1977) 113-122.

[51] F. Oppong, J. De Bruyn, Mircorheology and jamming in a yield-stress fluid, Rheologica acta 50(4) (2011) 317-326.

[52] F.K. Oppong, L. Rubatat, B.J. Frisken, A.E. Bailey, J.R. de Bruyn, Microrheology and structure of a yield-stress polymer gel, Physical Review E 73(4) (2006) 041405.

[53] E. Di Giuseppe, F. Corbi, F. Funiciello, A. Massmeyer, T. Santimano, M. Rosenau, A. Davaille, Characterization of Carbopol® hydrogel rheology for experimental tectonics and geodynamics, Tectonophysics 642 (2015) 29-45.

[54] I.A. Gutowski, D. Lee, J.R. de Bruyn, B.J. Frisken, Scaling and mesostructure of Carbopol dispersions, Rheologica acta 51(5) (2012) 441-450.

[55] J. Carnali, M. Naser, The use of dilute solution viscometry to characterize the network properties of carbopol microgels, Colloid and Polymer Science 270(2) (1992) 183-193.

[56] J.-Y. Kim, J.-Y. Song, E.-J. Lee, S.-K. Park, Rheological properties and microstructures of Carbopol gel network system, Colloid and Polymer Science 281(7) (2003) 614-623.

[57] Y. Liu, D. Lorusso, D.W. Holdsworth, T.L. Poepping, J.R. de Bruyn, Effect of confinement on the rheology of a yield-stress fluid, Journal of Non-Newtonian Fluid Mechanics 261 (2018) 25-32.

[58] J. Paredes, M.A. Michels, D. Bonn, Rheology across the zero-temperature jamming transition, Physical review letters 111(1) (2013) 015701.

[59] M. Dinkgreve, J. Paredes, M. Michels, D. Bonn, Universal rescaling of flow curves for yield-stress fluids close to jamming, Physical Review E 92(1) (2015) 012305.

[60] M. Dinkgreve, M. Michels, T. Mason, D. Bonn, Crossover between athermal jamming and the thermal glass transition of suspensions, Physical Review Letters 121(22) (2018) 228001.

[61] F. Chayes, The relation between area and volume in micrometric analysis, Mineralogical Magazine and Journal of the Mineralogical Society 30(221) (1953) 147-149.

[62] W.Y. Shih, W.H. Shih, I.A. Aksay, Elastic and yield behavior of strongly flocculated colloids, Journal of the American Ceramic Society 82(3) (1999) 616-624.

[63] R. D'Apolito, A. Perazzo, M. D'Antuono, V. Preziosi, G. Tomaiuolo, R. Miller, S. Guido, Measuring interfacial tension of emulsions in situ by microfluidics, Langmuir 34(17) (2018) 4991-4997.

[64] C. Caiazza, V. Preziosi, G. Tomaiuolo, D. O'Sullivan, V. Guida, S. Guido, Flow-induced concentration gradients in shear-banding of branched wormlike micellar solutions, Journal of colloid and interface science (2018).

[65] B. Mohebbi, A.H. Tavangarrad, J. Claussen, B. Blümich, S.M. Hassanizadeh, R. Rosati, Revealing how interfaces in stacked thin fibrous layers affect liquid ingress and transport properties by single-sided NMR, Journal of Magnetic Resonance 294 (2018) 16-23.

[66] E. Younes, M. Himl, Z. Stary, V. Bertola, T. Burghelea, On the elusive nature of Carbopol gels:“model”, weakly thixotropic, or time-dependent viscoplastic materials?, Journal of Non-Newtonian Fluid Mechanics (2020) 104315.

[67] P. Lefrançois, E. Ibarboure, B. Payré, E. Gontier, J.F. Le Meins, C. Schatz, Insights into C arbopol gel formulations: Microscopy analysis of the microstructure and the influence of polyol additives, Journal of Applied Polymer Science 132(46) (2015).

[68] R. Graziano, V. Preziosi, D. Uva, G. Tomaiuolo, B. Mohebbi, J. Claussen, S. Guido, The microstructure of Carbopol in water under static and flow conditions and its effect on the yield stress, Journal of Colloid and Interface Science 582 (2021) 1067-1074.

[69] N. Taylor, S. Gordon, Shear modulus in closely packed gel suspensions, Journal of Applied Polymer Science 27(11) (1982) 4377-4386.

[70] M. Cloitre, R. Borrega, L. Leibler, Rheological aging and rejuvenation in microgel pastes, Physical Review Letters 85(22) (2000) 4819.

[71] J.M. Smith, H. Van Ness, M. Abbott, M. Swihart, Introduction to chemical engineering thermodynamics (Eight Edition), McGraw Hill, 2018.

[72] A.V. Dobrynin, Phase diagram of solutions of associative polymers, Macromolecules 37(10) (2004) 3881-3893.

[73] P.J. Lu, E. Zaccarelli, F. Ciulla, A.B. Schofield, F. Sciortino, D.A. Weitz, Gelation of particles with short-range attraction, Nature 453(7194) (2008) 499-503.

[74] A. Zaccone, H. Winter, M. Siebenbürger, M. Ballauff, Linking self-assembly, rheology, and gel transition in attractive colloids, Journal of Rheology 58(5) (2014) 1219-1244.

[75] J. Gaume, H. Löwe, S. Tan, L. Tsang, Scaling laws for the mechanics of loose and cohesive granular materials based on Baxter's sticky hard spheres, Physical Review E 96(3) (2017) 032914.

[76] S. Van Vlierberghe, V. Cnudde, P. Dubruel, B. Masschaele, A. Cosijns, I. De Paepe, P.J. Jacobs, L. Van Hoorebeke, J.P. Remon, E. Schacht, Porous gelatin hydrogels: 1. Cryogenic formation and structure analysis, Biomacromolecules 8(2) (2007) 331-337.

[77] A. Poumaere, M. Moyers-González, C. Castelain, T. Burghelea, Unsteady laminar flows of a Carbopol® gel in the presence of wall slip, Journal of Non-Newtonian Fluid Mechanics 205 (2014) 28-40.

[78] P. Lidon, L. Villa, S. Manneville, Power-law creep and residual stresses in a carbopol gel, Rheologica Acta 56(3) (2017) 307-323.

[79] R. D'Apolito, F. Taraballi, S. Minardi, X. Liu, S. Caserta, A. Cevenini, E. Tasciotti, G. Tomaiuolo, S. Guido, Microfluidic interactions between red blood cells and drug carriers by image analysis techniques, Medical engineering & physics 38(1) (2016) 17-23.

[80] R. D'Apolito, G. Tomaiuolo, F. Taraballi, S. Minardi, D. Kirui, X. Liu, A. Cevenini, R. Palomba, M. Ferrari, F. Salvatore, Red blood cells affect the margination of

microparticles in synthetic microcapillaries and intravital microcirculation as a function of their size and shape, Journal of Controlled Release 217 (2015) 263-272.

[81] A.Y. Malkin, S. Patlazhan, Wall slip for complex liquids–Phenomenon and its causes, Advances in colloid and interface science 257 (2018) 42-57.

[82] P. Panaseti, A.-L. Vayssade, G.C. Georgiou, M. Cloitre, Confined viscoplastic flows with heterogeneous wall slip, Rheologica Acta 56(6) (2017) 539-553.

[83] V. Preziosi, G. Tomaiuolo, M. Fenizia, S. Caserta, S. Guido, Confined tube flow of low viscosity emulsions: Effect of matrix elasticity, Journal of Rheology 60(3) (2016) 419-432.

[84] A. Perazzo, L. Sicignano, G. Tomaiuolo, R. Marotta, R. Andreozzi, S. Guido, Tuning crystal structure in a micro-scale reactive flow, Chemical Engineering Science 207 (2019) 581-587.

[85] L. Sicignano, G. Tomaiuolo, A. Perazzo, S.P. Nolan, P.L. Maffettone, S. Guido, The effect of shear flow on microreactor clogging, Chemical Engineering Journal 341 (2018) 639-647.

[86] A. Zaccone, D. Gentili, H. Wu, M. Morbidelli, Shear-induced reaction-limited aggregation kinetics of Brownian particles at arbitrary concentrations, The Journal of chemical physics 132(13) (2010) 134903.

[87] F. Mura, A. Zaccone, Effects of shear flow on phase nucleation and crystallization, Physical Review E 93(4) (2016) 042803.

[88] M. Daneshi, A. Pourzahedi, D. Martinez, D. Grecov, Characterising wall-slip behaviour of carbopol gels in a fully-developed poiseuille flow, Journal of Non-Newtonian Fluid Mechanics 269 (2019) 65-72.

[89] S.P. Meeker, R.T. Bonnecaze, M. Cloitre, Slip and flow in pastes of soft particles: Direct observation and rheology, Journal of Rheology 48(6) (2004) 1295-1320.

[90] L. Isa, R. Besseling, A.B. Schofield, W.C. Poon, Quantitative imaging of concentrated suspensions under flow, High Solid Dispersions, Springer2010, pp. 163-202.

[91] R.T. Bonnecaze, M. Cloitre, Micromechanics of soft particle glasses, High Solid Dispersions, Springer2010, pp. 117-161.

[92] S. Caserta, M. Simeone, S. Guido, Shear banding in biphasic liquid-liquid systems, Physical review letters 100(13) (2008) 137801.

[93] A.H. Tavangarrad, B. Mohebbi, S.M. Hassanizadeh, R. Rosati, J. Claussen, B. Blümich, Continuum-scale modeling of liquid redistribution in a stack of thin hydrophilic fibrous layers, Transport in porous media 122(1) (2018) 203-219.

[94] L. Lanotte, G. Ausanio, M. Carbucicchio, V. Iannotti, M. Muller, Coexistence of very soft magnetism and good magnetoelastic coupling in the amorphous alloy Fe62. 5Co6Ni7. 5Zr6Cu1Nb2B15, Journal of magnetism and magnetic materials 215 (2000) 276-279.

[95] L. Lanotte, G. Ausanio, V. Iannotti, G. Tomaiuolo, L. Lanotte, Torsional oscillation monitoring by means of a magnetoelastic resonator: modeling and experimental functionalization to measure viscosity of liquids, Sensors and Actuators A: Physical 295 (2019) 551-559.

[96] P. R Varges, C. M Costa, B. S Fonseca, M. F Naccache, P.R. de Souza Mendes, Rheological characterization of carbopol® dispersions in water and in water/glycerol solutions, Fluids 4(1) (2019) 3.

[97] P. Møller, A. Fall, D. Bonn, Origin of apparent viscosity in yield stress fluids below yielding, EPL (Europhysics Letters) 87(3) (2009) 38004.

[98] V. Iannotti, L. Lanotte, G. Tomaiuolo, G. Ausanio, R. Graziano, L. Lanotte, An alternative approach for measuring yield stress and its application in Carbopol microgel, Rheologica Acta (2021).

[99] C. Hill, J. Eastoe, Foams: From nature to industry, Advances in colloid and interface science 247 (2017) 496-513.

[100] J.J. Bikerman, Foams, Springer Science & Business Media2013.

[101] R. Prud'homme, Foams: Theory: Measurements: Applications, Routledge2017.

[102] G.a.U.V.a.M.R. Gochev, Foams, (2000).

[103] R. Farajzadeh, A. Andrianov, R. Krastev, G. Hirasaki, W.R. Rossen, Foam–oil interaction in porous media: implications for foam assisted enhanced oil recovery, Advances in colloid and interface science 183 (2012) 1-13.

[104] I. Cantat, S. Cohen-Addad, F. Elias, F. Graner, R. Höhler, O. Pitois, F. Rouyer, A. Saint-Jalmes, Foams: structure and dynamics, OUP Oxford2013.

[105] P.A. Gauglitz, F. Friedmann, S.I. Kam, W.R. Rossen, Foam generation in homogeneous porous media, Chemical Engineering Science 57(19) (2002) 4037-4052.

[106] D.L. Weaire, S. Hutzler, The physics of foams, Oxford University Press2001.

[107] D. Exerowa, P.M. Kruglyakov, Foam and foam films: theory, experiment, application, Elsevier1997.

[108] W. Drenckhan, A. Saint-Jalmes, The science of foaming, Advances in colloid and interface science 222 (2015) 228-259.

[109] F. Wang, Z. Li, H. Chen, Q. Lv, W. Silagi, Z. Chen, Fractal characterization of dynamic structure of foam transport in porous media, Journal of Molecular Liquids 241 (2017) 675-683.

[110] Q. Sun, Z. Li, J. Wang, S. Li, L. Jiang, C. Zhang, Properties of multi-phase foam and its flow behavior in porous media, RSC Advances 5(83) (2015) 67676-67689.

[111] V.S. Ajaev, G. Homsy, Modeling shapes and dynamics of confined bubbles, Annu. Rev. Fluid Mech. 38 (2006) 277-307.

[112] K. Ma, R. Farajzadeh, J.L. Lopez-Salinas, C.A. Miller, S.L. Biswal, G.J. Hirasaki, Non-uniqueness, numerical artifacts, and parameter sensitivity in simulating steady-state and transient foam flow through porous media, Transport in porous media 102(3) (2014) 325-348.

[113] A.N. Fried, Foam-drive process for increasing the recovery of oil, Bureau of Mines, San Francisco, Calif.(USA). San Francisco Petroleum Research Lab., 1960.

[114] R. Kil, Q.P. Nguyen, W.R. Rossen, Determining trapped gas in foam from CT images, SPE Annual Technical Conference and Exhibition, Society of Petroleum Engineers, 2009.

[115] A. Kovscek, H. Bertin, Foam mobility in heterogeneous porous media, Transport in Porous Media 52(1) (2003) 17-35.

[116] J. Hou, Q. Du, Z. Li, G. Pan, X. Lu, K. Zhou, Experiments on foam texture under high pressure in porous media, Flow Measurement and Instrumentation 33 (2013) 68-76.

[117] A. Falls, G. Hirasaki, T.e.a. Patzek, D. Gauglitz, D. Miller, T. Ratulowski, Development of a mechanistic foam simulator: the population balance and generation by snap-off, SPE reservoir engineering 3(03) (1988) 884-892.

[118] H. Hematpour, S.M. Mahmood, S. Akbari, A.S. Asl, Foam modeling approaches in enhanced oil recovery: A review, Indian Journal of Science and Technology 9(22) (2016).

[119] H. Hematpour, S.M. Mahmood, N.H. Nasr, K.A. Elraies, Foam flow in porous media: Concepts, models and challenges, Journal of Natural Gas Science and Engineering (2018).

[120] G. Mary, S. Mezdour, G. Delaplace, R. Lauhon, G. Cuvelier, F. Ducept, Modelling of the continuous foaming operation by dimensional analysis, Chemical Engineering Research and Design 91(12) (2013) 2579-2586.

[121] J. Wang, A.V. Nguyen, S. Farrokhpay, A critical review of the growth, drainage and collapse of foams, Advances in colloid and interface science 228 (2016) 55-70.

[122] J. Hinze, Fundamentals of the hydrodynamic mechanism of splitting in dispersion processes, AIChE Journal 1(3) (1955) 289-295.

[123] D.A. Edwards, H. Brenner, D.T. Wasan, A.M. Kraynik, Interfacial Transport Processes and Rheology, Physics Today 46 (1993) 63.

[124] B.A. Schrefler, R. Scotta, A fully coupled dynamic model for two-phase fluid flow in deformable porous media, Computer methods in applied mechanics and engineering 190(24-25) (2001) 3223-3246.

[125] A. Khoei, T. Mohammadnejad, Numerical modeling of multiphase fluid flow in deforming porous media: A comparison between two-and three-phase models for seismic analysis of earth and rockfill dams, Computers and Geotechnics 38(2) (2011) 142-166.

[126] R. Graziano, V. Preziosi, G. Tomaiuolo, K. Braeckman, S. Guido, Experimental investigation on foam formation through deformable porous media, The Canadian Journal of Chemical Engineering 98(9) (2020) 2008-2015.

[127] V. Preziosi, A. Perazzo, G. Tomaiuolo, V. Pipich, D. Danino, L. Paduano, S. Guido, Flow-induced nanostructuring of gelled emulsions, Soft Matter 13(34) (2017) 5696-5703.

[128] F. Wang, Z. Li, H. Chen, X. Zhang, Establishment and application of a structure evolution model for aqueous foam based on fractal theory, RSC Advances 7(7) (2017) 3650-3659.